A 3D SERS DEVICE FOR HIGHLY SENSITIVE DETECTION OF ORGANIC CHEMICALS IN LIQUID

by

SANKGEETH VENNILA SIGAMANI

Presented to the Faculty of the Graduate School of

The University of Texas at Arlington in Partial Fulfillment

of the Requirements

for the Degree of

MASTER OF SCIENCE IN MATERIALS SCIENCE AND ENGINEERING

THE UNIVERSITY OF TEXAS AT ARLINGTON

May 2021

Acknowledgements

First off, I would like to thank Dr. Yaowu Hao, for his guidance, instructions, and encouragement throughout my research work from the beginning to end. I am proud to have worked under him and thanks to the opportunity he provided me. His kindness and encouragement kept me motivated.

I would like to thank Dr. Erika La Plante and Dr. Kyungsuk Yum for serving on my committee and for their valuable and knowledgeable evaluations, which helped me constructively in this research.

I would like to acknowledge the UTA Characterization Center for Materials and Biology (CCMB) lab and Dr. Jiechao C. Jiang, the facility manager. Without this facility, this study could not have been accomplished.

I would especially like to thank Aseem Athavale for training me and guiding me with this project. His technical expertise and support were essential ingredients to this study.

Finally, I would like to thank Shami Jose for believing in me and pushing me throughout, and my family for their love and support throughout my studies.

May 11th, 2021

Abstract

A 3D SERS DEVICE FOR HIGHLY SENSITIVE DETECTION OF ORGANIC CHEMICALS IN LIQUID

Sankgeeth Vennila Sigamani, M.S

The University of Texas at Arlington, 2021

Supervising Professor: Yaowu Hao

Detection of organic chemicals in liquid medium have been gaining utmost attention in recent times. Real time detection and monitoring of a variety of environmental pollutants, explosive materials, chemical agents, and pharmaceutical drugs in liquid medium are of great need in today's technological advancements. While there are several scattering, emission and spectroscopy techniques in use, Raman spectroscopy is attractive because of its molecular specificity i.e., each molecule has a Raman fingerprint. Raman spectroscopy utilizes the inelastic portion of the scattered wave for detection. But since intensity of inelastic scattering (Raman scattering) is very low, compared to the elastic scattering, low concentration analysis has been challenging.

Surface-Enhanced Raman spectroscopy or Surface-Enhanced Raman Scattering (SERS) potentially overcomes this challenge, with its

good detection capabilities for lower concentrations in liquid solution. SERS enhances the Raman signal of molecules (capable of 10^{10}-fold enhancement) when they are adsorbed on a metal nanostructure (termed as SERS substrate) surface. The design of SERS substrate plays a crucial part in the enhancement of the Raman signal. Conventional 2D substrates are not very efficient in providing binding of the analyte molecules to SERS-sensitive hotspots and in-situ detection can be challenging, owing to the low volume of liquid on the surface. These challenges can be overcome by using three-dimensional (3D) hierarchical nanostructures as SERS substrates, because of its high hotspot density along all spatial directions.

Single crystal 3D silver dendrites are desirable for such application, due to the presence of nanotips and nanogaps which act as hotspots enhancing the Raman signal. These silver nano dendrites can be generated by a simple Galvanic Replacement Reaction (GRR) between copper wire and silver nitrate solution, yielding a multi-level branched nanostructure. These branched surfaces in proximity, have the capability to enhance the Raman signal of the analyte present, due to Localized Surface Plasmon Resonance effect (LSPR).

In this thesis, a reliable, reusable and low-cost SERS device, employing 3D silver nano dendrites, that can be used for in-situ monitoring of organic molecules in liquid flows is presented. This device has the capability to detect very low concentrations of organic chemicals, at parts per million range in liquid in real time, without much of an erroneous

measurement and sample preparation. The device was made of 3D silver nano-dendrites enclosed in channels in PDMS. It is reusable, with good reproducibility and has the potential for multichannel configurations that can provide parallel analysis. This device is made reliable by calibrating using Rhodamine-6g, as a reference molecule. It can be then used to detect various Raman active molecules in liquid solution with varying concentrations.

We detected molecules of 4-Mercaptobenzoic Acid (4- MBA) and Methylene blue in liquid solutions with very low concentrations. Detection of Acetaminophen and Thiabendazole with good reproducibility, makes the device to have significant potentials at real-world applications in different fields. The device was successful in detecting ultra-low concentrations with high sensitivity, as compared to previously reported nano substrates thus making it a significant SERS substrate.

Table of contents

List of figures

Chapter 1

Introduction

Detection of organic chemicals in liquid at PPM concentrations, within minutes and with few or no false-positive responses, is sought after in many different applications and industries. Gas Chromatography coupled Mass Spectrometry (GC/MS) [1, 2, 3, 4, 5], Ion Mobility Spectrometry (IMS) [6, 7], Infrared Spectroscopy (IR), Raman spectroscopy [8, 9, 10, 11, 12, 13], etc. are some common techniques used for the analytical determination of organic chemicals. All the fore mentioned measurements are typically carried out by sampling, extraction, and separation of the chemical mixtures from the aqueous matrix. The liquid samples may also undergo chemical and physical transformations during this process, which may lead to inaccurate results. Also, these methods require complex equipment, extended time and laborious operations. For example, GC/MS has been used to detect 0.02 ppm analytes in water, but the analysis required as much as an hour to perform [5]. Although in efforts of solving equipment complexity, portable Infra-Red and Raman spectrometers have been developed, but only 100 ppm analytes in water were measured using Infrared spectroscopy and 5000 ppm analytes in chloroform were measured using Raman spectroscopy [9, 13].

Surface-Enhanced Raman Spectroscopy (SERS) overcomes the above limitations and greatly increases the sensitivity [14]. SERS is a technique which determines enhanced Raman signal from Raman active molecules, that are adsorbed to the surface of an appropriate metal nanostructure. Such massive intensification of the Raman

scattering from molecules rise from Localized Surface Plasmon Resonance (LSPR) effect, supported by metal nanostructures [15]. Scattering efficiencies increase by as much as 14 orders of magnitude, when the target analytes interact with the surface-plasmon modes of metal particles, although 10 orders of magnitude are more common. It has become a very important tool for chemical analysis, environmental applications, and biological sensing due to its high levels of sensitivity and high spectroscopic precision [16]. Detection is accurate and obtained with or without any sample preparation, and as less as a single molecule can be detected [17, 18, 19, 20]. SERS techniques share the advantages of conventional Raman spectroscopy, such as low background signals [21], specific signals for particular molecules [22] and multiplexing capabilities [21]. SERS can also be utilized to detect and monitor certain environmental pollutants, explosive materials, chemical agents, and pharmaceutical drugs in flowing liquid media [23, 24, 25].

However, one of the important limitations of SERS application is the difficulty in statistical binding of analyte to the surface of SERS hot spot [26, 27, 28, 29, 30]. Hence, it becomes extremely tough and tricky to detect highly diluted solutions in liquid media. To overcome this problem, it is important to design and develop a robust SERS substrate with high reproducibility and high hotspot density. The synthesis process of the substrate should also be easy, not time consuming, of low cost and with minimal usage of hazardous chemicals.

In the past few years, the ability of SERS has grown to measure organic chemicals in liquid, with sufficient spectral uniqueness. A silver-coated microsphere and electrochemically roughened gold or silver foil have been reported to be used as efficient SERS substrates [31, 32, 33]. They were used to analyze several organic chemicals and

achieved significant spectral enhancement. However, the sample solution needed to be dried on the substrates to obtain sensitivity at 0.05 ppm. Another SERS substrate, formed by templated self-assembly of gold nanoparticles has been used to detect 0.04 ppm cyanide in a liquid medium [34]. But it required an acid wash to get optimum sensitivity and the measurements were also irreversible. Silver-doped sol-gels were developed as SERS active medium and were coated on the inside walls of glass vials that hold the liquid samples [35]. However, they were not able to detect very low concentrations. Recently, chloroform covered by gold nanorods inside a glass cuvette, serving as a SERS substrate has been reported to be used in detecting pesticides [36]. But the process included lots of hazardous chemicals for substrate synthesis and surface treatments.

The above-mentioned drawbacks can be overcome with three-dimensional (3D) metal nano dendrites as SERS substrates. It is a hierarchical nanostructure, containing multiple branched structures, that can increase the Raman signal by providing more hotspots created at the tip of these branches, as well as at the junctions [37]. Moreover, high surface area of the dendritic structure can also provide more interaction between the substrate and the analyte molecules. Considering these factors, nano dendrites made of noble metals like silver (Ag) are exceptional candidates for use as SERS substrates, as they show excellent electrical conductivity and Localized Surface Plasmon Resonance (LSPR) properties.

As of today, there are numerous synthesis processes reported to develop Ag hierarchical nanostructures, with diverse structural features and applications. These include several deposition reactions, evaporation reactions, redox reactions, templated synthesis using reducing agents and light irradiation techniques. Most of the methods that

are developed to synthesis silver dendrites has one or more deficiencies including, but not limited to laborious processes, adulterated substrates, high cost, low-yield restrictions, and poor reproducibility. For example, when the dendrites are generated by templated synthesis, to detach them from the templates special care must be taken [38]. One simple method that can overcome the shortcomings stated above is using a Galvanic Replacement Reaction (GRR) to synthesis dendritic nano structures. GRR is driven by the difference between the reduction potential of the target metal and a sacrificial metal.

In this research, we designed a simple, low cost, and reusable device that employs 3D Ag dendrite nanostructures for enhancing Raman signal, for the detection of organic chemicals in liquid medium with significant reproducibility and commercial potentials. Ag nano dendrites were synthesized by GRR, inside the channels made of the polydimethylsiloxane (PDMS), which serves as a 3D SERS substrate. The dendrite is produced by a GRR between a copper wire and silver nitrate solution which is a simple, cost effective and fast method. The size and shape effect of the generated dendrites are studied theoretically using a Finite Difference Time Domain (FDTD) simulation. We demonstrated that this SERS device can be calibrated by using Rhodamine-6g as a reference molecule and can be employed for detection of 4-Mercaptobenzoic Acid (4-MBA), Methylene blue, Acetaminophen and Thiabendazole in liquid solutions with various concentrations. The results indicated that the 3D nanostructures can amplify Raman signals for extremely low concentrations of these molecules with consistent, rapid, and reproducible SERS results.

Chapter 2

Background information

2.1 Raman scattering theory

The scattering of light can be thought of as the deviation of an electromagnetic (EM) wave (i.e., light ray) as it runs into a material with non-uniformity or an obstacle [39]. When the EM wave of frequency υ_o, interacts with the material, the electron orbits are disturbed periodically with the frequency same as that of the electric field of the incident wave, illustrated in Figure 1. A dipole moment is induced when the charges in the orbit are separated, and the electron cloud oscillates periodically within the molecule. Thus, the material gets polarized. Because of this polarization the material gets to an excited state and in turn scatters light [40]. When light is scattered by a material, most of it are elastically scattered (Rayleigh scattering), where the scattered photons have the same energy (frequency, wavelength, and color) as that of the incident light but travel in different directions. However, a small portion of light is scattered at a different frequency. This scattering is referred to as inelastic scattering also called Raman scattering [41].

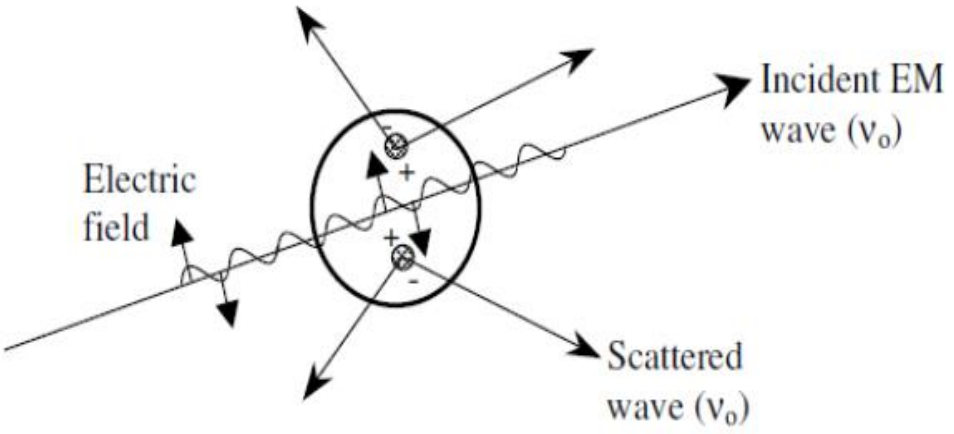

Figure 1: Interaction of Electromagnetic (EM) wave with a material [41]

As stated previously, an induced dipole moment is generated when an incident EM light wave interacts with a material. The induced dipole moment, P, is given by

$$P = \alpha \bar{E} \quad (1)$$

where α is the polarizability of the material and E is the intensity of the electric field of the incident light source. Material properties like the molecular structure and nature of the bonds determine the polarizability of the material.

For the incident EM wave, the electric field can be expressed as

$$\bar{E} = E_0 \cos(2\pi \nu_0 t) \quad (2)$$

where υ_o is the frequency (Hz) of the incident EM wave.

The time-dependent induced dipole moment can be obtained by substituting equation (2) in (1),

$$P = \alpha\, E_0 \cos(2\pi \nu_0 t) \quad (3)$$

The polarizability is a function of the instantaneous position of constituent atoms since the relative position of the individual atoms determine the ability to disturb the local electron cloud of a molecular structure.

For any molecular bond, the individual atoms are confined to specific vibrational modes, in which the vibrational energy levels are quantized in a manner like electronic energies. A particular mode of vibrational energy is given by

$$E_{vib} = \left(j + {}^{1}/_{2}\right)h\nu_{vib} \qquad 4$$

where j is the vibrational quantum number (j = 0,1,2…), υ_{vib} is the frequency of the vibrational mode, and h is the Planck's constant.

The physical displacement dQ of the atoms about their equilibrium position due to the vibrational mode may be expressed as

$$dQ = Q_0 \cos(2\pi\nu_{vib}t) \qquad 5$$

where Q_o is the highest limit displacement about the equilibrium position.

For small displacements, the polarizability may be approximated by Taylor expansion as,

$$\alpha = \alpha_0 + \frac{\partial\alpha}{\partial Q}dQ \qquad 6$$

where α_o is the polarizability of the material when its molecular vibrational mode is at equilibrium position.

Based on the vibrational displacement of Equation (5), the polarizability may be given as

$$\alpha = \alpha_0 + \frac{\partial\alpha}{\partial Q}Q_0 \cos(2\pi\nu_{vib}t) \qquad 7$$

Finally, Equation (7) may be substituted in Equation (3), which yields

$$P = \alpha_0 \, E_0 \, cos(2\pi\nu_0 t) + \frac{\partial \alpha}{\partial Q} \, Q_0 \, E_0 \, cos(2\pi\nu_{vib} t) \, cos(2\pi\nu_0 t) \quad (8)$$

The above relation may be recast as

$$P = \alpha_0 \, E_0 \, cos(2\pi\nu_0 t) + \left(\frac{\partial \alpha}{\partial Q} \frac{Q_0 E_0}{2}\right) \{\cos[2\pi(\nu_0 - \nu_{vib})t] \cos[2\pi(\nu_0 + \nu_{vib})t]\} \quad (9)$$

This equation indicates that induced dipole moments are created at three different frequencies, ν_0, (ν_0−ν_{vib}), and (ν_0+ν_{vib}), which in return produce scattered radiation at these same three frequencies. The first scattered frequency, ν_0, represents elastic scattering as it has the same frequency as that of the incident light. However, the latter two frequencies, (ν_0−ν_{vib}), and (ν_0+ν_{vib}), are inelastic because of their shifts and are considered as Raman scattering. The down-shifted frequency is known as Stokes scattering, where the molecule does not relax back to the original ground state and some vibrational energy is transferred to the molecule, resulting in emission of a longer wavelength. The up-shifted frequency known as anti-Stokes scattering, where the molecule originally in the excited vibrational state comes back to a lower energy state, resulting in emission of a shorter wavelength.

From the equation (9) the necessary condition for Raman scattering is that the term $\frac{\partial \alpha}{\partial Q}$ must be non-zero. Polarizability changes when the vibrational displacement of atoms corresponds to particular vibrational modes. For example, consider a diatomic molecule A-B, with maximum vibrational displacement Q_o.

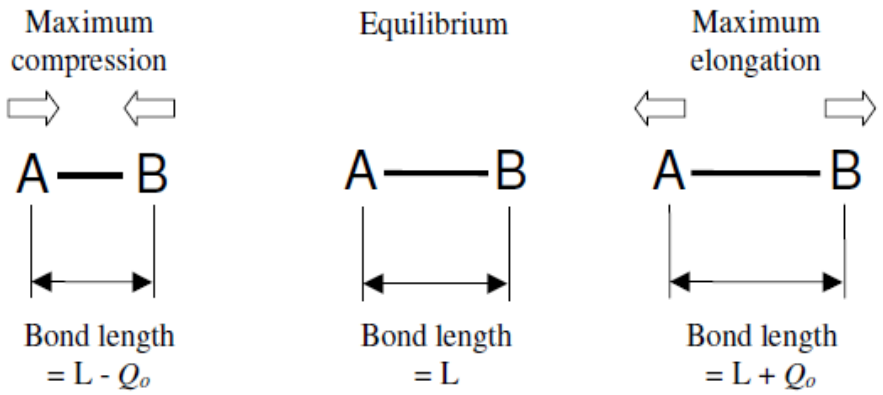

Figure 2: Vibrational displacement of A-B about the equilibrium position [42]

As depicted in Figure 2, when A-B are in maximum compression, their electrons will have attraction from nucleus of the other atom, and hence it will be very difficult to perturb electrons in this situation. So, the polarizability will be minimum. On the contrary, when atoms A-B are at maximum displacement, electrons can be easily perturbed. Hence polarizability will be the highest in this situation. However, it should be noted that polarizability is continuously changing with respect to the displacement of the atoms.

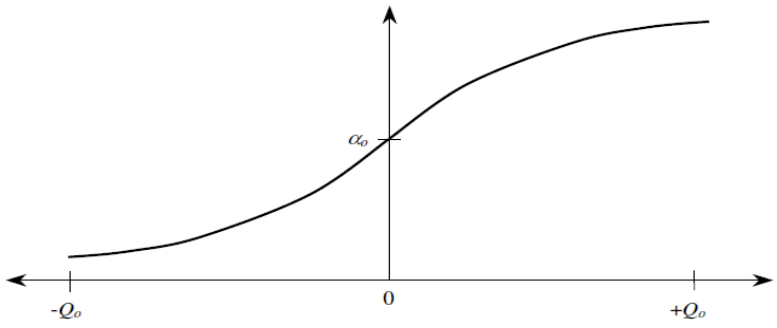

Figure 3: Polarizability of A-B as a function of vibrational displacement about equilibrium [42]

In Figure 3 $\partial\alpha/\partial Q$ is non-zero, throughout the range which satisfies the Raman condition. Hence the system will produce Raman scattering at the two frequencies ($\nu_0-\nu_{vib}$) and ($\nu_0+\nu_{vib}$).

2.2 Raman spectroscopy

Raman microscope is a commonly used materials characterization instrument. Raman microscopy is not primarily used for imaging purposes and thus, it can also be referred to as Raman micro-spectroscopy. This instrument often called micro-Raman, is of the dispersive type, which means it collects spectrum at each wave number separately. This microscope can observe tiny areas of materials by focusing the laser beam down to the micrometer level without much sample preparation, if a surface of the sample is free from contamination.

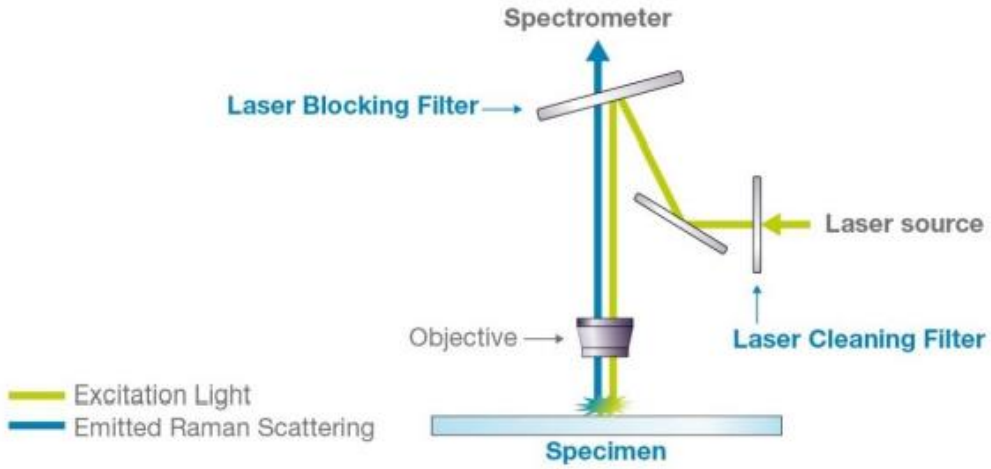

Figure 4: Schematic diagram of Raman spectrometer

(adopted from Raman Filters - Optical Filters for Raman Spectroscopy. (n.d.)., from this website)

The optical arrangement of a Raman microscopic system is schematically illustrated in Figure 4. A single-wavelength beam is generated by passing a laser beam through a cleaning filter. This beam is then focused on the sample surface by the microscope. The Raman scattered light, reflected from a small area of the sample is collected by the microscope and sent to the detector. A holographic filter is used to block the laser light from entering the detector system along with the inelastically scattered light. Before being recorded by a detector, the wavelength of Raman scattering light is chosen by a diffraction grating system.

Typical Raman microscope includes the following elements

- Laser source.
- Sample illumination and collection system.
- Spectral analyzer.
- Detection and computer control and processing system

In 1960s the field of Raman spectroscopy was revolutionized due to the development of lasers. It is easy to create a high-fluence and narrow-excitation region within a small volume of sample by focusing the laser beam. This smaller region could be easily coupled optically onto the entrance slit of a spectrometer. Raman spectroscopy uses laser as an excitation source, providing highly monochromatic light. The excitation laser source generates laser beams with wavelengths in the visible light range or closer to it. A commercially available and regularly used Raman excitation laser is the He-Ne laser (638.2nm) [43]. Other commonly used laser sources are gas continuous-wave lasers such as Ar^+, Kr^+, etc. These laser sources are often capable of generating beams of multiple wavelengths. For example, Ar^+ generates a range of wavelengths with different

intensities of 515.4 nm, 488.0nm, and 350.7nm. If we are using Ar^+ laser with a specific wavelength, it is necessary to filter out all the other wavelengths.

The major difference between the microscope used in the Raman system and the conventional ones used for observation of microstructure is that Raman microscope only needs to illuminate a target area and not the entire field. The high numerical aperture microscope is used to collect the Raman-scattered light over a large solid angle effectively. The schematic layout in Figure 5 illustrates the optical features of the Raman microscope. A single monochromatic wavelength is obtained by allowing the laser beam to pass through a laser cleaning filter. The appearance of diffraction rings and speckle noise from around the focused spot is removed by a slit. This ensures a defined laser beam for illumination. This laser beam is then reflected by a beam splitter and goes through an objective lens to illuminate the sample. After illumination, the Raman-scattered light from the sample is collected by a wide-aperture objective lens and focused on another adjustable slit placed in the image plane of the microscope. Both the slits are called confocal diaphragms, because they are in exact optical conjugation positions with respect to the point source on the sample surface, like the confocal aperture in a confocal microscope. The purpose of this confocal arrangement is to make sure that the light transmitted to the spectral analyzer and detector is originated only from the focused small area of the sample. These two slits are important for both illuminating the sample and collection of Raman-scattered light. They increase the spatial resolution by eliminating stray light coming from the region of the sample that is not in focus. As low as 1μm of spatial resolution can be reached for the sample by adjusting the slit diaphragm, when using a 100× objective lens.

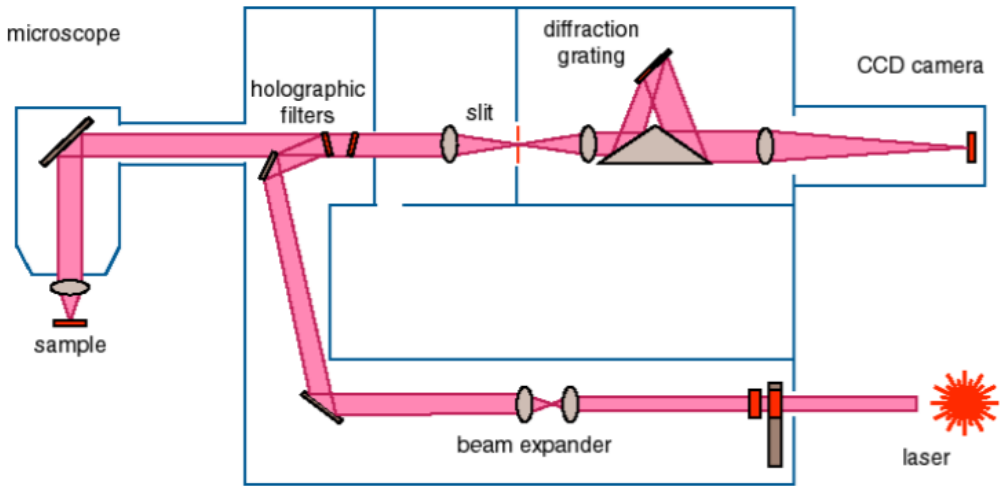

Figure 5: Optical diagram of a Raman microscope [43]

The inelastically scattered Raman light has intensity lower than that of the elastically scattered light. So, it requires a special filter to block the elastically scattered light. Hence, before the scattered light from the sample reaches the spectral analyzer, a special filter is used to remove elastically scattered light. This filter possesses a ‘‘notch’’ like feature, which is the zero-transmission range for a specific wave number, aligned to be the exciting laser wave number and thus eliminating it. The filtered inelastically scattered light then reaches the diffraction grating, which is the key component of the spectral analyzer in the Raman microscope. The objective of diffraction grating is to disperse the Raman-scattered light according to its wave numbers. The surface of diffraction grating consists of equally spaced fine parallel grooves. Based on Bragg’s Law of diffraction, Raman scattered light incident on the diffraction grating, is dispersed by diffracting in distinct directions depending upon the incident wavelength. The role of diffraction grating in Raman spectroscopy is exactly same as that of equally spaced

atomic planes in crystals, which diffracts different wavelengths in different angles. Usually, a range of 1000 wave numbers can be covered by one diffraction grating. In recently developed Raman microscopes, the diffraction grating can continuously rotate and change its angle with respect to the incident Raman scattered light. This ensures recording Raman spectrum with a range of 400–4000cm^{-1} and separates different wave numbers smoothly. A spectral resolution of 1cm^{-1} can be obtained by the diffraction grating.

The Raman scattered light which is separated according to the wavelength is recorded by a detector, that is made of photoelectric materials. This detector converts photon signals to electric signals. The detector used in Raman spectroscopy is mostly a multichannel and solid-state device. The Charge-Coupled Device (CCD) is the most used Raman detector. It is a silicon-based semiconductor arranged as an array of photosensitive elements. A simple one-dimensional array of CCD can detect and record light intensity of distinct wavelengths, separated by the diffraction grating. The Stokes scattered Raman shift is calculated and plotted versus the wave number in the Raman spectrum by computer processing.

Fluorescence can be seen in impure samples. This is because the impurities in the sample may absorb laser radiation and re-emit it as fluorescence. This fluorescence has an intensity that can be as much as 10^6 times higher than that of Raman scattered light. Thus, a Raman spectrum can be completely covered by the fluorescence. This causes a major drawback of using Raman spectroscopy. To minimize fluorescence issues in the sample, the following three methods are commonly used [43]:

- The sample is irradiated with high-power laser beams for a prolonged time.

- Near infrared (longer wavelength) excitation laser source is used as it has less excitation energy of the laser beam, thus reducing the chance of fluorescence.
- Pulsed laser source like electron gate can be used to measure Raman signal and to reduce fluorescence because the lifetime of Raman scattering (10^{12} s to 10^{10} s) is much shorter than that of fluorescence (10^{-9} s to 10^{-7} s).

2.3 Surface-Enhanced Raman Scattering

Raman scattering has low intensity than elastic scattering, making it hard to detect the Raman light for low concentration of molecules. It has been found that, if analyte molecules that are to be detected, are adsorbed on a plasmonic metal nanoparticle surface, the weak Raman scattering signal can be drastically enhanced. This effect of enhancement is known as Surface-Enhanced Raman Scattering (SERS). SERS was first observed by Fleischman et al. in 1974 [44]. It was then confirmed by Van Duyne, Jeanmarie [45] and Albrecht, Creighton [46] independently that, when molecules were adsorbed on a roughed silver substrate, the Raman signals were enhanced about a million times. Shortly afterward, Martin Moskovits in 1978 first explained that the unusual increase in Raman cross section was because of the presence of excited surface plasmons [47, 48]. Nowadays, SERS has advanced a lot. It has become a powerful tool to detect trace amounts of molecules in the order of 10^{-14} to 10^{-15} M concentrations. More importantly, it has also triggered the development of near-field optics [49] and other novel devices based on plasmon [50].

The effect of SERS enhancement is related to and can be explained by both electromagnetic [51, 52, 53, 54, 55, 56, 57] and electronic mechanisms [58, 59, 60, 61, 62, 63, 64]. But electromagnetic enhancement is the major mechanism. The electromagnetic theorem states that the field enhancement occurs due to the resonant effect, between the optical fields and the surface plasmon in the metal. This leads to the redistribution of electric field intensities around the metal surface. Therefore, the Raman signals can be massively enhanced when the molecules are near or on the metal surface. This enhancement depends on the type, size, shape, and arrangement of the metal particles and the frequency of the incident light [65]. When both the incident and scattering fields are resonated with the plasmon frequency, the enhancement becomes exceptionally strong.

2.3.1 Localized Surface Plasmon Resonance

SERS enhancement occurs due to the electromagnetic enhancement mechanisms which can be explained by Localized Surface Plasmon Resonance (LSPR) phenomenon. An applied external electric field i.e., light, when shined on the surface of the metal, causes the free electrons on the surface to move back and forth collectively. This gives rise to surface plasmon due to the polarization of electrons. These negatively charged free electrons on vibration, produces an electric field. Coherent vibration of the electric field from the oscillation of free electrons and the applied external electric field (e.g., electromagnetic waves), results in the phenomenon referred to as Surface Plasmon Resonance (SPR) which occurs at the surface of the metal [66]. Also, the resonance

frequency would shift from the plasma frequency to the SPR frequency. For most metals, the plasma frequency is seen in the ultraviolet (UV) region. Normally, the frequency shift between the incident light and Raman scattering is very small compared to the width of plasmon resonance. However, for some metals like Au, Ag, and Cu, the plasma shift frequency is near to the visible light zone.

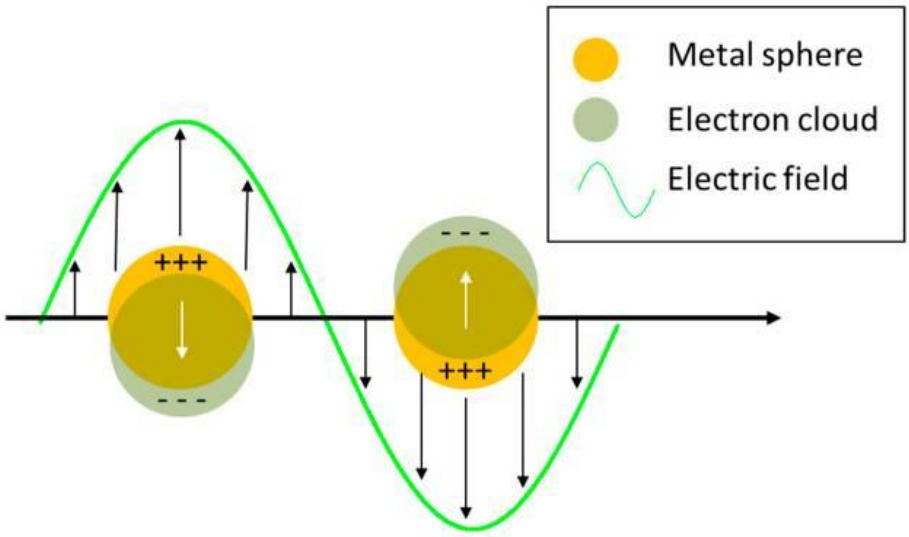

Figure 6: LSPR effect on the spherical nanoparticle [66]

When the electromagnetic field impinges on metal nanostructures with dimension much smaller than the wavelength of incident light, the collective oscillation of plasma would be localized near the surface. The absorption and scattering of the visible and near infrared (NIR) lights can be strongly enhanced by these nanoparticles at the Surface plasmon resonance frequency. This effect is termed as LSPR effect. In brief, LSPR is nothing but SPR in nanometer-sized structures. The interaction between the conduction electrons on the surface of the metal nanoparticle and the incident light results in the occurrence of this phenomenon [66]. Figure 6 illustrates the collective oscillations of

electrons in a spherical nanoparticle under the action of an external electric field. The term ‘localized’ indicates that the propagation of the oscillation of the electrons is limited. This is because of the size of the nanoparticles that are much smaller than the wavelength of light, making these oscillations spatially localized in three dimensions. Thus, when light wave is trapped inside the conductive metal nanoparticles (MNPs) with sizes smaller than wavelength of light, LSPR effect is observed. Since, LSPR is the resonation of the electric field from the localized oscillation of free electrons and the applied external electric field, the plasmon absorption intensity and position can be greatly affected by the surface property of the metal. Thus, by changing the size and structure of the material we can obtain different types of plasmonic modes [67]. Recently, plasmonic nanostructures are used with great potential in optical devices, bio-sensing, and SERS. It is well known that the size, shape, morphology, and crystallinity can affect the properties of plasmonic nanostructures [68].

The Raman signal of a molecule can be hugely enhanced when it resides near the metal surface, where both the particle’s polarization frequency and the illuminating light frequency resonates. The particle features like morphology and arrangement, and the frequency of the incident electromagnetic field determines the enhancement factor.

2.3.2 Electromagnetic enhancement

It has been found that SERS can have an enhancement factor that can reach up to $10^{15} – 10^{16}$ [69, 70, 71], although estimates of $10^{5} – 10^{10}$ are more common. The largest observed SERS signal is mainly due to the plasmon resonance enhancement which is an

electromagnetic enhancement mechanism. Electromagnetic enhancement mechanism has two contributions namely, local field (or near field) enhancement and re-radiation enhancement [51, 52, 53, 54, 55, 56, 57]. In local field enhancement, the contribution of the local electric fields around metal-particle surfaces are enhanced by plasmon excitation. This induces a strong spatial localization called “Hotspot”. Re-radiation enhancement is the second contribution to electromagnetic enhancement, where the efficiency of the molecule to radiate Raman signal is increased when it is near a metallic substrate. Oscillation of the molecule depends on the environment in which it is embedded. Particle size, shape, arrangement, and dielectric environment also have a strong sensitivity to SERS signal intensification in this electromagnetic enhancement mechanism. For the enhancement of the Raman signal to be effective, the molecule should be near the metal particle surface within 1-50nm distance [65,66].

In conventional Raman scattering, when the excitation laser radiation oscillating at angular frequency ω_L and electric field $E(\omega_L)$, irradiates a molecule, it is characterized by a Raman polarizability tensor $\alpha_R(\omega_R, \omega_L)$. The oscillating dipole at the Raman frequency is induced by the excitation light source. The radiated Raman intensity is proportional to the square modulus of the dipole. Whereas, in SERS electromagnetic enhancement, the molecule experiences the electric field of $E_{Loc}(\omega_L)$ when it is placed near a plasmonic metal substrate. This electric field experienced by the molecule is much stronger than the input excitation light source $E(\omega_L)$. The emitted Raman scattering intensity is also enhanced by the presence of the plasmonic metal nano substrate. Thus, both the input laser source and the output Raman signal are enhanced when the molecule is near the

plasmonic metal nano structure. Then the total electromagnetic enhancement is approximated to $|E|^4$.

Based on this phenomenon, the enhancement factor in a molecule is given by

$$E(\omega_R) = |E_0(\omega_L)|^2 \, |E(\omega')|^2 \qquad 1$$

where $E_0(\omega_L)$ is the local electric-field at the incident angular frequency ω_L and $E(\omega')$ is the corresponding factor at the Stokes-shifted frequency ω'.

Equation (1) is the most used expression that is employed to get the numerical values of the enhancements. In conventional SERS, $E(\omega_R)$ can be averaged and is often approximated by assuming that $E_0(\omega_L)$ and $E(\omega')$ are the same at the surface area of the metal nano particles, where molecules can adsorb to generate the observed enhancement factor $\langle E(\omega_R) \rangle$, and therefore equation (1) becomes

$$E(\omega_R) = |E_0(\omega_L)|^4 \qquad 2$$

The plasmon width is large compared to the Stokes shift, which this approximation takes as an advantage.

The easiest way to figure out and quantify the local field enhancement is to utilize the classical view of Raman scattering.

The external electric field ($E_0(\omega_L)$) produced by the laser oscillating at ω_L, induces an oscillating dipole ($p(\omega_R)$) in the molecule at the Raman angular frequency ω_R.

$$P_m(\omega_R) = \alpha_{R,\,m}(\omega_R, \omega_L)\, E_0(\omega_L) \qquad 3$$

Where $\alpha_{R\,m}(\omega_R, \omega_L)$ is the Raman polarizability tensor of the molecule.

Similarly for the particle,

$$P_p(\omega_R) = \alpha_{R,\,p}(\omega_R, \omega_L)\, E_0(\omega_L) \qquad 4$$

Where $\alpha_{R,\,p}(\omega_R, \omega_L)$ is the Raman polarizability tensor of the particle.

The molecule near the metallic substrate experiences a huge local electric field (E_{Loc} (ω_L)) that is stronger than the input field (E_0 (ω_L)), due to the polarization of the particle. This leads to the increment of the incident field ($E_0 + E_{loc}$). The incident light intensity is proportional to $(E_0+E_{0,\ loc})^2$. Equation 2 indicates that the electric field is proportional to the enhancement. The increased incident field then excites the analyte molecule which can emit Raman scattered light.

The emitted field from a molecule, E_{mol}, is also enhanced by polarization of metal particles giving rise to a total field of $E_{mol} + E_{mol,loc}$. The Raman intensity is now approximately $(E_{mol}+E_{mol,loc})^2$. Therefore, the Raman signal is enhanced by E^2 at every stage.

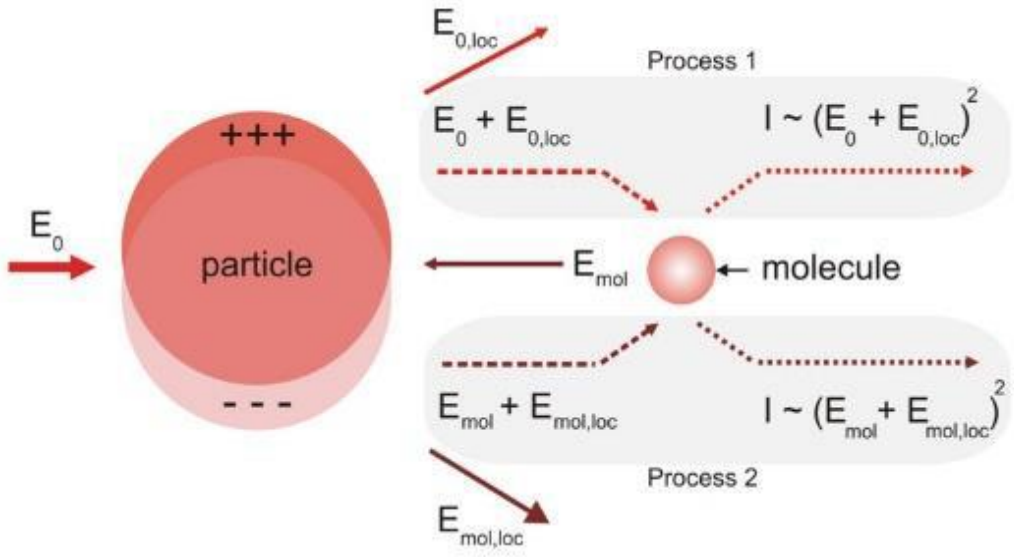

Figure 7: Schematic representation of SERS electromagnetic enhancement

(Surface-Enhanced Raman Scattering. (n.d.)., from this website)

As the analyte molecule is very close to nanoparticle surface, the induced dipole field of the particle (E_p=CP$_p$) can be added to the incident field for the calculation of the

dipole moment of the molecule (C is a constant). Similarly, the induced dipole field from the molecule (E_m=CP$_m$) can be added to the incident field when identifying the dipole moment for the particle. Thus, the coupled dipole system becomes:

$$P_p = \alpha_p(E_0 + CP_m) \quad (5)$$

$$P_m = \alpha_m(E_0 + CP_p) \quad (6)$$

Upon solving this system, we get

$$P_p = \alpha_p\,(1 + C\alpha_m / 1 - C^2\alpha_p\alpha_m)\,E_0 = \alpha_p{}^o E_0 \quad (7)$$

$$P_m = \alpha_m\,(1 + C\alpha_p / 1 - C^2\alpha_p\alpha_m)\,E_0 = \alpha_m{}^o E_0 \quad (8)$$

Where, $\alpha_p{}^o$ and $\alpha_m{}^o$ are the effective polarizability of the particle and the molecule, respectively. Since LSPR at the particle surface shows that α_p >> α_m, near the particle surface the effective polarizability of the particle ($\alpha_p{}^o$) dominates the system.

The local field enhancement can be defined as:

$$G = \frac{I_{SERS}}{I_{Raman}} \quad (9)$$

$$\frac{I_{SERS}}{I_{Raman}} = \left[\frac{C\alpha_p + C^2\alpha_p^2}{(1 - C^2\alpha_p\alpha_m)^2}\right]^2 \approx (C\alpha_p)^4 \approx \left|\frac{E_{loc}}{E_0}\right|^4 \quad (10)$$

Therefore, the 4th power of the ratio between the field near the nanoparticle and the incident field can be achieved [66,72].

The metal nanostructures for SERS should have the dimensions that cannot be smaller than analyte molecules and the wavelength of the excitation light to achieve the surface enhancement [47]. If the nanostructures become too small to gain lower dimensional limit, conductivity of the MNPs reduce drastically due to electronic scattering

at the particle's surface [73, 74, 75]. In response, reradiated field will be reduced in strength and the quality of dipolar resonance will also be compromised. The upper dimensional limit of the particles is determined by the wavelength. Larger size cannot generate dipolar plasmon which is responsible for SERS enhancement. Generally, the size ranges from 5nm to 100nm.

Nowadays, there are more theoretical enhancement estimates by using computational electrodynamics methods such as Discrete Dipole Approximation (DDA) [76] and Finite Difference Time Domain (FDTD) [77] calculation. These methods can be used for non-resonant molecules on the surface of the nanoparticles, by solving Maxwell's equations to determine the local fields E(ω). Any size and shape of the particle can be used in these methods, as they represent the nano structures using finite elements. For nanoparticles, the enhancement can be calculated for a large number of particles but are limited to the total number of elements needed to converge the calculation as finite elements. However, coupled multipole expansions can be used to pair many particles together.

2.3.3 Hotspots

For a SERS-active system to be effective it must contain nanostructures or nanofeatures. These characteristics have an advantage of providing high field enhancement. The distribution of the local field enhancement at the surface of a plasmonic metal substrate is highly nonuniform. It is mainly localized in very small spatial regions called "hot spots". Sharp tips and nanogaps are often considered as hot spots in

a structural point of view. Nanogaps are nothing but the very small gap between the nanoparticles or between a nanoparticle and a surface [78, 79]. When the molecules are contained within the confined volume of nano features, an approximate increase of 10^{10} times in Raman signal can be achieved.

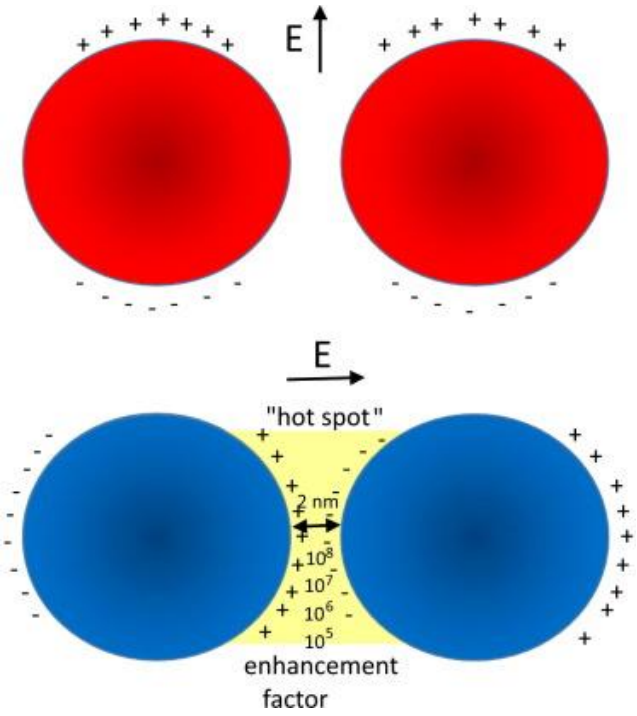

Figure 8: Effect of orientation of vector-E with respect to hotspots [19]

The illustration in Figure 8 explains that if two MNPs placed within the range of 1-50nm is excited by using an appropriate light source, strength of the hotspot is greatly increased. This high level of increase is seen only if the external electric field is aligned with the axis connecting the two MNPs. This is due to the polarization of the nanoparticles; an excess of positive and negative charges is generated on the opposite sides of the metal nanoparticles by the applied external electric field. The strength of hotspot will be

reduced if the distance between these MNPs increase. It is also noted that there will be no significant enhancement effect on molecules, if the excitation light source is having an electric field aligned perpendicular to the axis of the nanoparticles. In this situation no hotspots can be observed even if the distance between nanoparticles is reduced. This is because, the induced dipoles are oriented in a way that allows no mutual reinforcement.

Thus, the polarization of both the nanoparticles is increased as a result of reciprocal interaction between them. Hence there exists a combined effect of both the external field and the polarization of the charges induced by the nearby nanoparticle, acting on each of the two nanoparticles. In other words, the polarization of one nanoparticle is contributed not only by the external electric field, but also by the induced dipole from the next nanoparticle. The individual polarization of each nanoparticles also influences the molecule placed in between them. Thus, decreasing the distance between the two nanoparticles drastically increases the capacitive field on the molecule placed between them.

The enhancement can be strongly increased by reducing the gap size (g). Approximately 10^5 times enhancement has been achieved at g = 10nm and 10^9 times at g = 2nm for two gold nanoparticles of radius 25nm [72]. The enhancement is approximately given by $1/g^2$ and is termed as the power law dependence [80]. But for a single gold sphere the enhancement factor is approximately only 10^3 which explains the reason that SERS is mostly observed on aggregated nanoparticles and hardly on isolated nanoparticles. The nanogaps are more efficient than the sharp tips in amplifying the Raman signals because of this reason. For few cases like hollow nanoparticles, the field enhancement generated between the nanoparticles may be neutralized by a cutback of

the field inside the nanoparticles, thus even the aggregation of this structure weakly enhances the Raman scattering [81]. And for gap sizes less than 1nm the SERS enhancement is limited due to quantum mechanical phenomena like electron tunneling [82].

2.4 SERS substrate

The very crucial topic in SERS research is the fabrication of SERS active substrate. The main features like arrangement and morphology of the nano particles and the frequency of the incident excitation light source affects the enhancement of the Raman signal. The MNPs made of silver, gold, and copper with different sizes and shapes can be used for this purpose. Producing SERS substrates with competent characteristics like high uniformity, reproducibility, and sensitivity is of high importance to efficiently obtain SERS enhancement. There are lots of hot research to discover different synthesis methods of MNPs in different nanostructures, by controlling the size and shape of the metal nanostructures in 1, 2 and even in 3 dimensions.

We know that the Raman enhancement phenomenon occurs when the analyte molecules adsorb to the hotspots in the SERS substrate. Thus, one of the important principles in the design of the SERS substrate is to create as greater number of hotspots as possible. The overall efficiency of the Raman enhancement is critically dependent upon the dimensions of metal nanostructures. They should neither be large and nor too small to generate significant Raman enhancement. For quantitative measurements, these features are important [66].

A robust SERS substrate should not only possess the above discussed abilities, but it should have high stability, ease of fabrication, low cost of production etc. It is found that the 3D metal nanostructures with well-regulated hierarchical morphologies are good candidates as highly effective SERS substrates. Compared with conventional SERS substrates, it is possible that the hotspots can be expanded along the third dimension in the 3D metal nanostructure. In addition, large number of analyte molecules to be detected, can be adsorbed on the substrate due to the large surface area.

Generally, 3D SERS substrates are fabricated by two principal strategies. One is 3D self-assembly method and the other is template method. In 3D self-assembly method, the assembly of the nanostructures are done by two techniques, the top-down technique and bottom-up technique. In the top-down approach, lateral patterning of bulk materials is formed into nano-sized structures either by subtractive or additive methods. Most of the lithography techniques, laser machining, nanocontact printing, deposition, ion implantation and diffusion used to fabricate nanostructures are using the top-down approach. In the bottom-up approach, desired nanostructures are assembled by controlled segregation of atoms or molecules. Plasma arcing, solgel method, metal organic decomposition, chemical vapor deposition processes, molecular beam epitaxy, wet syntheses, laser pyrolysis and self-assembly processes utilize the bottom-up approach. But this technique suffers from poor control, poor reproducibility, imperfection in the processed material, high cost and longer processing times. In the template method, 3D nano scaffolds are used as a template to make nanostructures with noble MNPs. Currently, by using template method many 3D SERS substrates have been widely developed. For example, the gold or silver nanoparticles decorated Anodic Aluminum

Oxide (AAO) channels [83], carbon nanotubes (CNTs) [84], titanium dioxide (TiO_2) nanoarrays [85], zinc oxide (ZnO) nanorod arrays [86] are some of the most notable 3D SERS substrates generated by templated synthesis. Figure 9 shows an illustration of a 3D SERS substrate [87].

Figure 9: Fractal Silver Dendrites as 3D SERS Substrate [87]

2.4.1 Silver nanoparticles for SERS substrate

MNPs with different sizes and shapes, made from noble metals like silver (Ag), gold (Au), copper (Cu) are widely used as SERS substrates. Ag nanoparticles are explored to be one of the most advantageous among various MNPs. A crucial property of Ag in terms of SERS is that it has a robust surface plasmonic effect. Also, among all other precious metals, silver is the cheapest. Because of these unique qualities of silver and the fact, it can be easily made into desired nanostructures, it has been extensively studied

[88]. By changing the size and shape of the Ag nanostructures we can easily alter its SERS properties. This led to the synthesis of various shape-controlled silver nanostructures like 0D-nano clusters, 1D-nanowires [89], 2D-nanoprisms [90], 3D-flower-like particles [91], 3D-nanosheet-assembled micro-hemispheres [92], 3D-nanorod arrays [93], to name a few.

2.5 Silver dendrites and its synthesis process

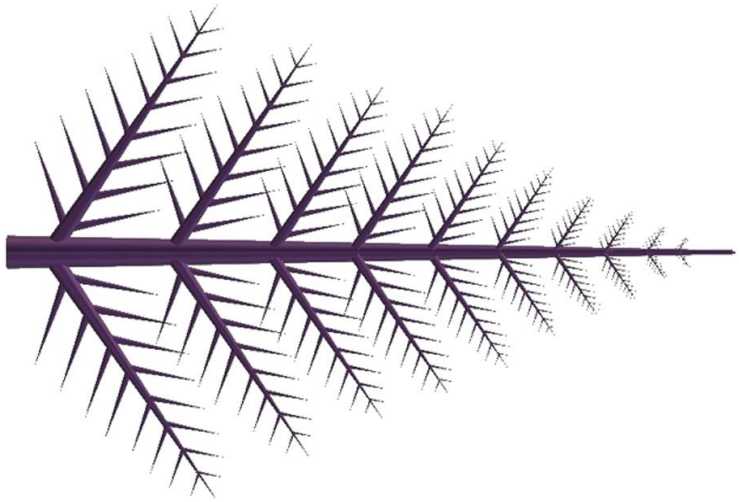

Figure 10: A simple dendritic structure with a base trunk containing primary and secondary branches [94]

Various nano shapes such as cubes, rods, wires, disks, triangles, prisms, and dendrites can be synthesized with Ag nanoparticles [95]. Among these many shapes, dendritic structures are important because of their unique features like high complex interfacial structure and large specific surface area. The dendrites are made of many multilevel hierarchical branches as illustrated in Figure 10. Owning to the complex

interfacial structure the target analyte molecules can easily be adsorbed to the surface. More importantly, the coupling of SPR of two adjacent branches of the dendrites creates a strong electromagnetic field when irradiated with excitation light source, creating hotspots with high enhancement. Therefore, silver dendrite conforms a substantial ability to be used as a SERS substrate [96, 97, 98, 99, 100, 101, 102].

Hierarchical silver nanostructures can be fabricated by various methods like electrochemical deposition [103, 104, 105, 106], electroless redox reaction [107, 108, 109], wet chemical synthesis using reducing agents in aqueous solution [110, 111, 112, 113], photocatalytic reduction [114, 115], decomposition by visible light irradiation [116], ultraviolet irradiation of surfactant micelles [117], ultrasonically assisted templated synthesis, iodination treatment to evaporated Ag foil surface [118], sono-electrochemical deposition [119, 120, 121], and photoreduction by ultraviolet irradiation [122]. But these synthesis methods have some limitations. Several of these methods are time consuming (which may take up to 1-30 days), a few needs special instruments, some uses extremely hazardous materials (e.g., HF); certain methods make use of seed particles and templates; quite a few require multiple capping agents and even multiple synthesis steps; also in more than a few methods, it is difficult to remove the templates from the surface of the products causing damage to the substrates; some have high-cost and low-yield restrictions.

2.5.1 Galvanic Replacement Reaction

Galvanic replacement techniques are also widely used to synthesize Ag nano dendrites, which avoid introduction of complex templates and chemicals into the reaction process. This simple, low-cost method can efficiently produce Ag nano dendrites in large scale with well-defined structures.

Galvanic Replacement Reaction (GRR) is a simple and attractive technique used to produce various noble metal (such as Au, Ag, Pd, and Pt) nanostructures and even their alloys. GRR is an electrochemical process in which, the ions of metal having higher reduction potential is used oxidize another sacrificial metal. This method has a partial ability to tune the shape, size, morphology, and composition of the resulting metal nanostructures [123]. In all the cases it is not easy to control the structure and morphology of the metal nanostructure to be fabricated. This is because it is very sensitive to the synthesis condition, temperature, comprising ion concentrations, and the original state of the sacrificial material. Several studies show that Ag nano dendrites can be formed by using a metal that is more reactive than silver as substrate (e.g., Cu [124, 125, 126, 127, 128], Mg [129], Al [130], Zn [131], Ni [132], Sn [133]). In most of these studies, the direct electron transfer, between the sacrificial substrate and Ag^{+} ions, is attributed to galvanic replacement (redox reaction). This causes the formation and growth of hierarchical silver nano dendrites on the surface of the metal substrate or onto the template containing the sacrificial material.

The formation of silver dendrites is explained by a galvanic reaction between copper and silver nitrate as follows.

Oxidation reaction: $Cu_{(s)} \rightarrow Cu^{2+}_{(aq)} + 2e^-$ (0.34 V vs. SHE)

Reduction reaction: $2\,Ag^+_{(aq)} + 2e^- \rightarrow 2Ag_{(s)}$ (0.80 V vs. SHE)

Electrons are generated in the oxidation reaction, which takes place at the copper surface, where both Cu^{2+} ions and the electrons are released into the solution. Ag^+ in the solution will get reduced to Ag on copper surface by accepting the electrons from the oxidation reaction. Therefore, each copper ion is replaced by two silver ions at the surface of copper. Figure 11, shows the schematic of galvanic replacement reaction between copper wire and silver nitrate for the silver dendrite formation process.

Overall reaction: $2AgNO_{3(aq)} + Cu_{(s)} \rightarrow Cu\,(NO_3)_{2(aq)} + 2Ag_{(s)}$

$$Cu_{(s)} + 2Ag^+_{(aq)} \rightarrow Cu^{2+}_{(aq)} + 2Ag_{(s)}$$

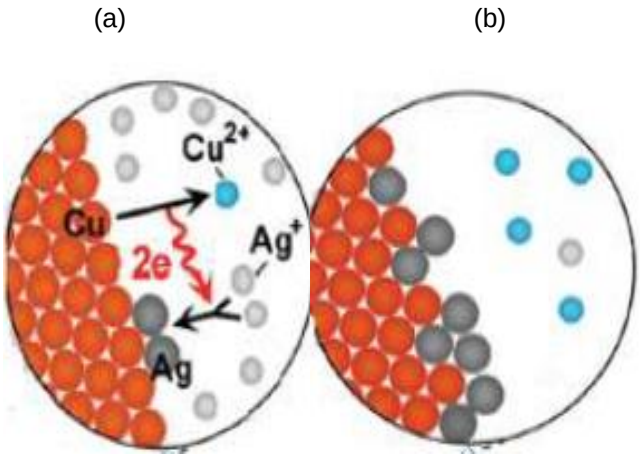

Figure 11: Schematics of Galvanic Replacement Reaction between surface of copper and silver nitrate solution for silver dendrite formation. (a) Replacement at the start of GRR process. (b) replacement after 1min of GRR process.

The growth of Ag dendrites can be explained by the anisotropic crystal growth and the Diffusion-Limited Aggregation (DLA) model. The thermodynamic factors and the inherent crystal structure of the material are responsible for the growth of the dendrite nanostructure by the GRR process. The rough surfaces like defects, stacking faults or steps are the spots where GRR is initiated. These spots are mostly high surface energy areas where the bulk energy of the total system tends to decrease. This makes the silver nanoparticles to accumulate dendritic rather than a hexagonal structure which is thermodynamically stable. Even though byproducts like small silver nanoparticles are also formed and mixed with the silver dendrites, it does not affect the properties of the dendritic structure.

Initially, the reduced silver atoms aggregate to form a nucleus. A stable nanocrystal can be formed by rapid growth of this nucleus. The facet of the nanocrystals is determined by the facet that minimizes the total surface energy. It has been observed and calculated that the lowest surface energy is found on multiply twinned decahedron with (111) facets [109]. There are lots of stable multiply twinned decahedron nanoparticles in the solution during nucleation stage. Thus, the dendrite embryo is generated when these nanoparticles can pile up together by oriented connection. This forms an elongated structure with (111) facets at the end and with protrusions on the sides. Several mechanisms like diffusion-limited aggregation, oriented attachment, and Ostwald ripening describes the subsequent growth of the branched aggregates of nanoparticles (dendrite embryo). Therefore, as the reaction progresses, Ostwald ripening gets some of the small nanoparticles to fade away, and some of them form single crystal silver dendrites as they might have enough time to relax and fuse to minimum energy positions. From the surface

of the copper, the electrons can reach above the deposited silver and also to the tip of the dendrites. The silver ions in the solution could obtain these electrons to grow silver atoms from the tip position. This mechanism is shown in Figure 12. As silver crystal growth prefers (111) direction, they can form single crystal silver dendrites.

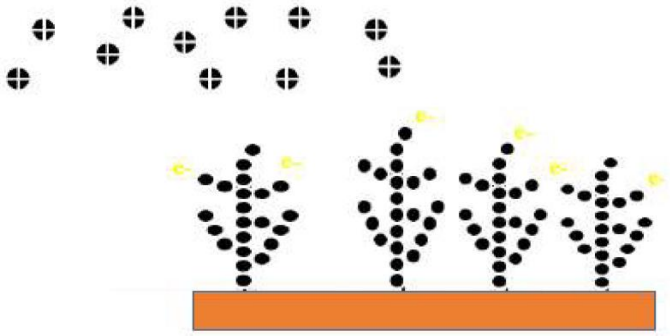

Figure 12: The mechanism of growth of silver dendrites on the surface of copper

The above-mentioned mechanism is for formation of dendrites on the surface of the copper, but not all dendrites are attached to the copper surface and some are free-standing without any connection with the copper. For GRR to take place, electrons must be transferred which requires metallic contact. But for the free-standing dendrites there is no contact between the metals. Since electrons cannot be transferred through the solution, this free-standing dendritic growth formation has to be attributed to the ions in the solution [38].

$$Cu_{(aq)} + NO_3^-{}_{(aq)} + 2\ H^+_{(aq)} \rightarrow Cu^{2+}_{(aq)}\ NO_2^-{}_{(aq)} + H_2O \quad (1)$$

$$Ag^+_{(aq)} + 2NO_2^-{}_{(aq)} + 2H_2O \rightarrow Ag_{(s)} + 2NO_3^-{}_{(aq)} + 4H^+ \quad (2)$$

The only stable and possible intermediate ion in the aqueous solution is NO_2^- (nitrite) ion. It is also found that copper can reduce nitrate ion to nitrite ion by reaction following the equation 1. This nitrite ion in turn reduces Ag^+ ion to Ag by following the reaction equation 2. This results in the formation of free-standing silver dendrites.

Chapter 3

Experiments and results

3.1 Materials and reagents

Sylgard 184 PDMS Base and Slygard 184 PDMS curing agent were purchased from Dow corning, Midland, MI. Two square geometry capillary tube with diameter 200µm and 500µm made of borosilicate glass were purchased from Vitrocom. $AgNO_3$ powder and Thiabendazole were purchased from Alfa Aesar (Ward Hill, MA, USA). Rhodamine-6g, 4-Mercaptobenzoic Acid (4-MBA), Methylene blue, and Acetaminophen were bought from Sigma Aldrich. Latex free syringe of 3 ml from BD medical and copper bus bar wire of 80µm was purchased from MSC industrial supply Co. Glass slides and small paper clips were purchased as stationary. Millipore system is used to purify the water that is used throughout all these experiments. All chemicals were used as received.

3.2 Synthesis of silver dendrites inside a capillary tube

Figure 13: Concentric capillary design

Capillary tube made of borosilicate glass with an inner diameter of 500µm that is referred as thick glass tube, and 200µm inner diameter tube, that can be called as thin

glass tube was used in this process. First, the copper bus bar wire, 20mm in length and 80µm in diameter is cleaned with acetone and deionized water to get rid of any contaminants or dust. This cleaned copper wire is inserted into the thick capillary glass tube followed by inserting the thin capillary, halfway into the thick glass capillary from both sides. This creates a tapered structure, which is illustrated in Figure 13. This concentric capillary design was made to hold the silver dendrites in a wedge, preventing them from getting washed away. This setup is connected to a syringe through a connector at one end leaving the other end undisturbed. All the connections between the capillaries and interface between the capillary and the connector are sealed with UV cured epoxy to prevent any leakage of solutions. This setup is then used to create silver dendrites inside the tube. Figure 14 shows the entire setup for the silver dendrites synthesis.

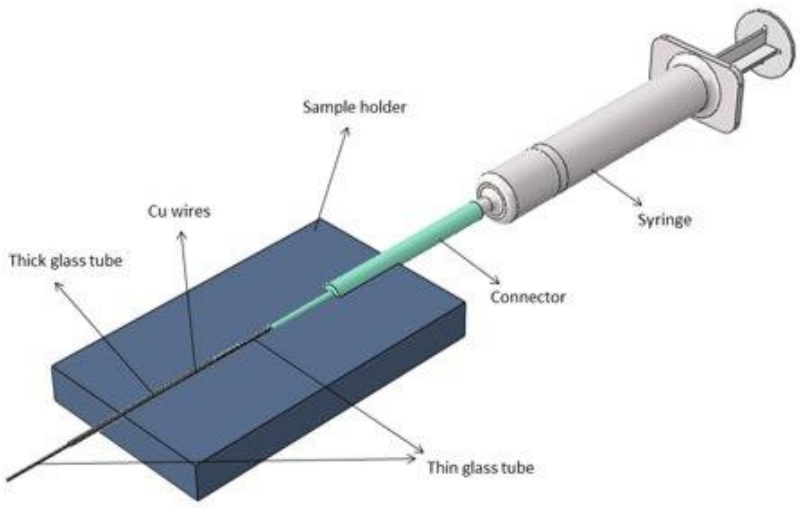

Figure 14: The complete experimental setup for synthesis of silver dendrites

An aqueous $AgNO_3$ solution of 0.1M concentration is prepared. 3ml of this solution is slowly injected through the capillary tube for 10 minutes using the syringe. Flowrate of 0.30ml/min in maintained. Silver nitrate reacts with the copper wire to form silver dendrites

due to galvanic replacement reaction. After the development of silver dendrites, 10ml of deionized water is slowly injected into the capillary tube for washing. Deionized water is passed very slowly and carefully to wash the capillary thoroughly without affecting the formed dendrites. This washing process is to remove excess solution and reaction byproducts such as AgCl inside the tube. Figure 15 shows the formed dendrites inside the thick glass capillary tube.

Figure 15: Silver dendrites formed inside the capillary glass tube

3.2.1 Characterization of silver dendrites inside the capillary glass tube

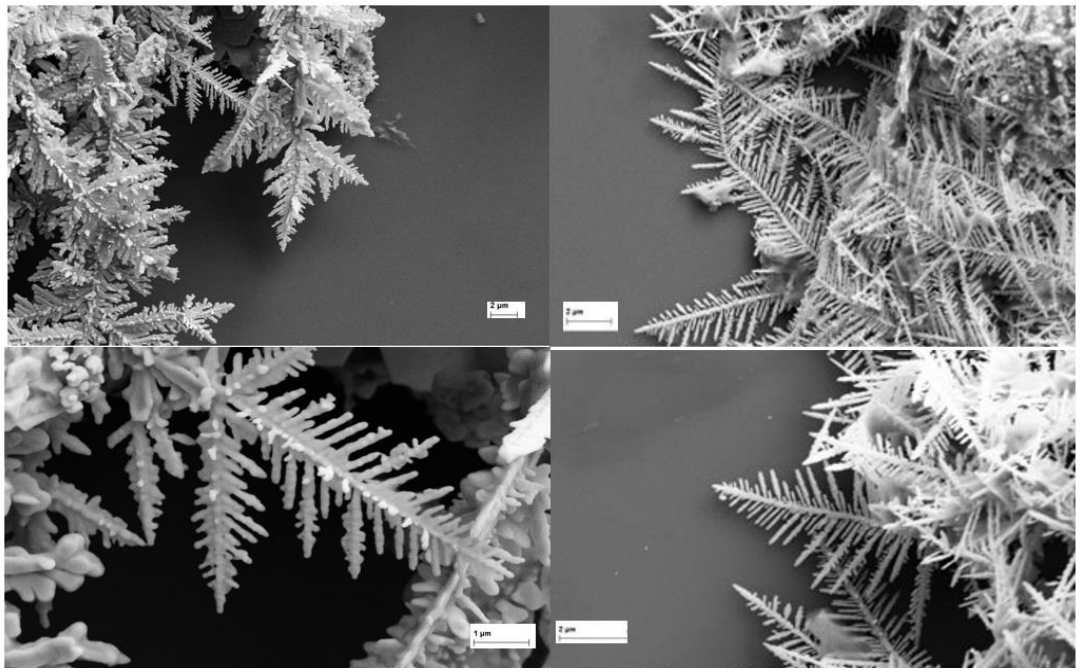

Figure 16: SEM images of silver dendrites formed inside capillary tube

Silver dendrites inside the capillary tube is characterized using Field Emission-Scanning Electron Microscope (SEM). From the SEM images in Figure 16, we can clearly see the well-defined dendritic structures.

3.2.2 SERS measurements

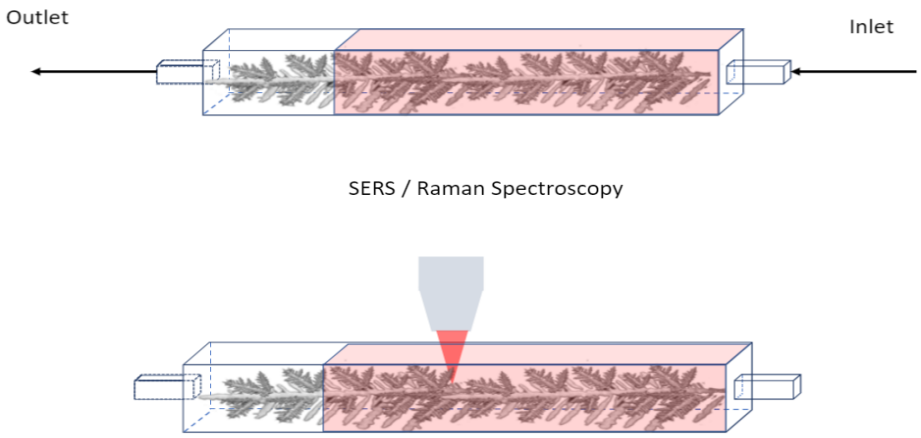

Figure 17: Schematic representation of the SERS measurements using capillary substrate

This capillary substrate with 3D silver dendrite can be used to enhance the Raman signal of the organic chemicals in liquid medium. The solution that is to be detected is injected into the capillary substrate using a syringe, till it reaches the other side. Careful consideration is made as to not overflow the solution beyond the other side of the capillary, as this can increase the concentration of the solution inside the capillary more than intended. The laser is focused on the dendrite as show in Figure 17 to detect the analyte molecules in liquid solution.

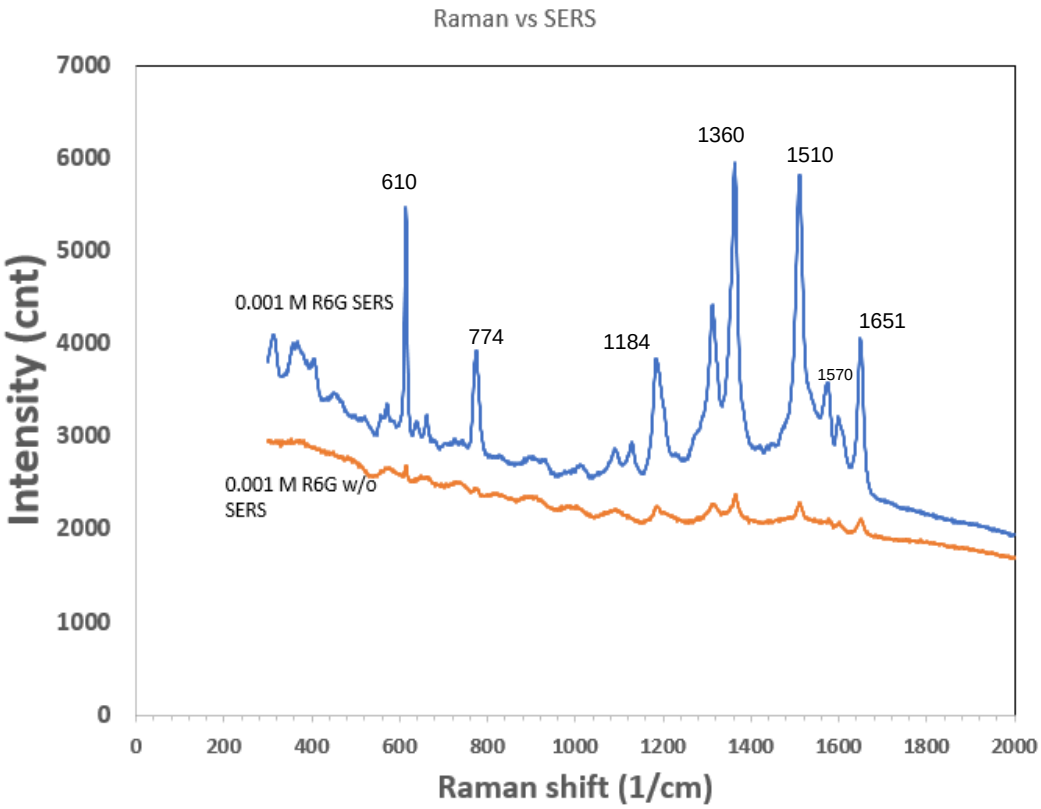

Figure 18: Enhancement effect of Ag dendrites in capillary glass tube

To prove SERS effect with the capillary substrate, we conducted analysis with and without the substrate using Rhodamine 6g (R6g), which is a common dye extensively used in the field of SERS. Raman spectra of 10^{-3} M R6g with and without the capillary substrate is represented in Figure 18. While detecting R6g in liquid without the substrate, the Raman signal obtained was weak with very low intensity. Using silver dendrite capillary substrate, significant enhancement was achieved. The characteristic Raman peaks for R6g are at 610, 767, 1184, 1360, 1510, 1570 and 1651cm^{-1}. These correspond to the C-C-C ring in-plane vibrations, C-H out of plane bending, C-H in-plane bending vibrations, C-O-C stretching and C-C stretching of ring respectively [134]. At 610cm^{-1} the

SERS intensity enhancement is approximately 1000 times, compared to Raman peaks without SERS substrate in liquid medium. Thus, it is deduced that silver dendrite in capillary as SERS substrate has the ability to significantly enhance Raman signal.

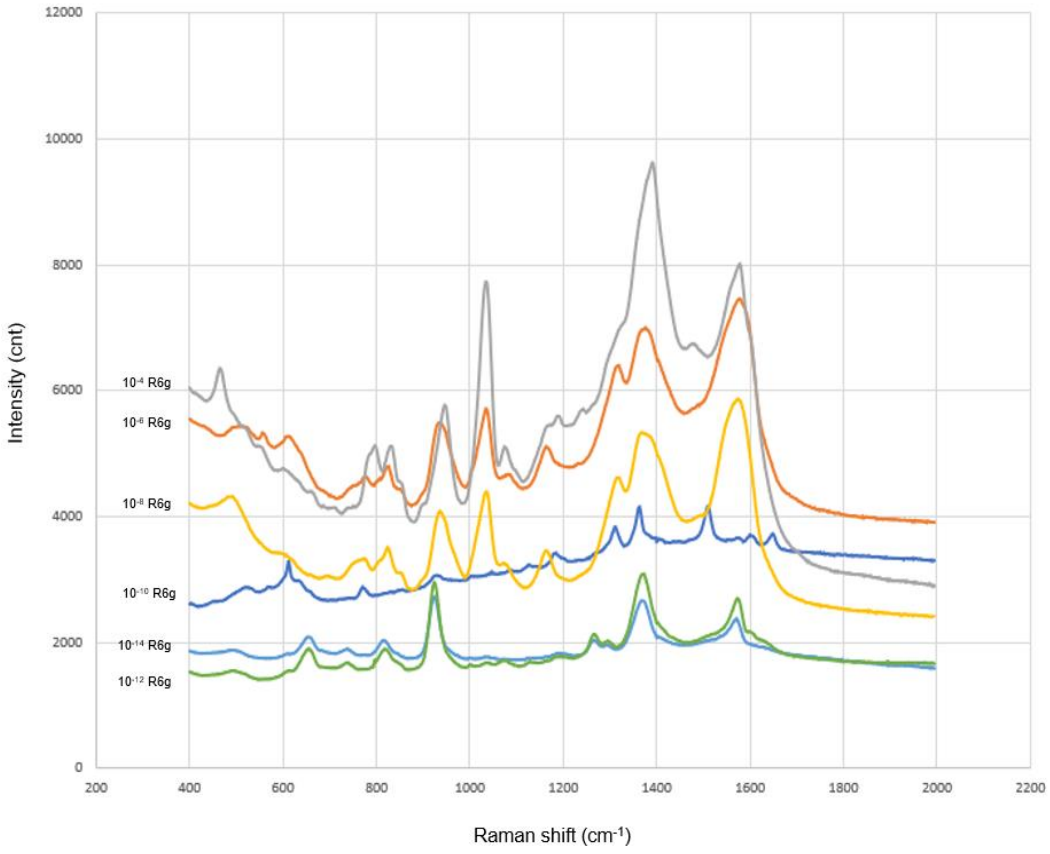

Figure 19: Raman spectrum for R6g solutions with concentrations in the range of 10^{-4} to 10^{-14} M using capillary substrate

Various low concentration solutions of R6g were made by diluting the stock solution, generating 10^{-4} to 10^{-14} M concentration solutions. R6g concentrations as low as 10^{-14} M were detected using the capillary substrates. Clearly defined peaks were observed, which are shown in Figure 19.

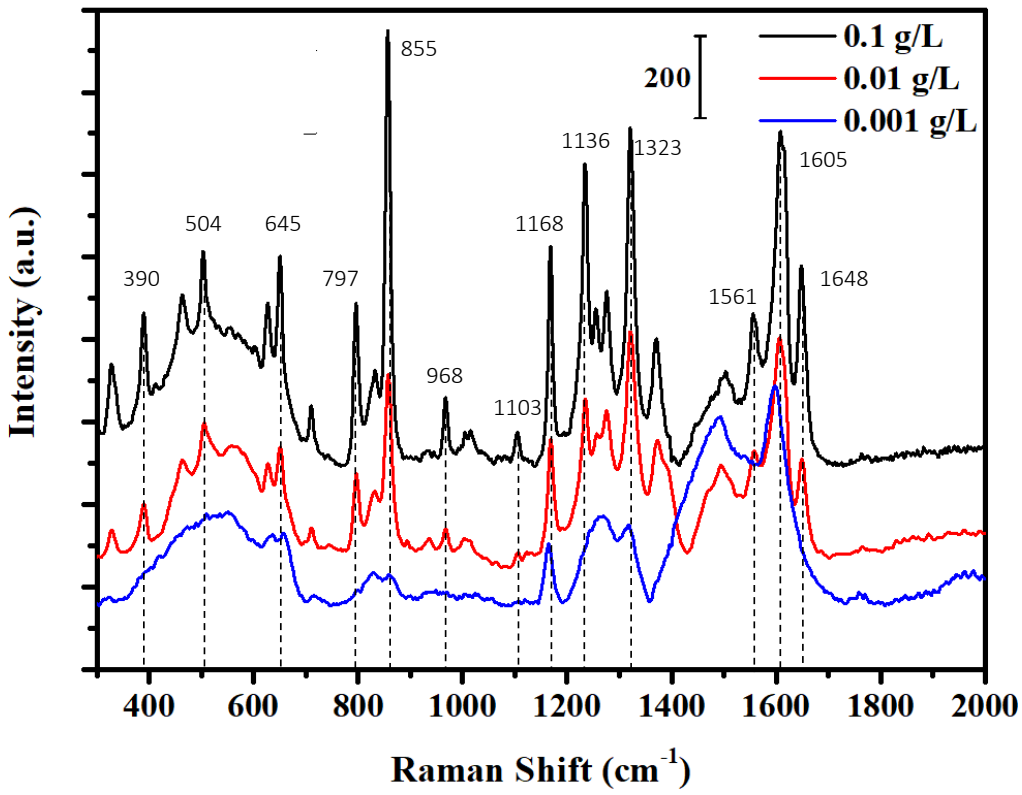

Figure 20: Raman spectrum for Acetaminophen in aqueous solution at 3 different concentration using capillary substrate

In view of potential practical applications, we tested the device for detection of acetaminophen which is commonly known as Tylenol used for fever relief. It is not a harmful drug, but overdose may lead to severe liver damage. Using this capillary substrate, concentrations as low as 1 ppm of acetaminophen in liquid solution was detected. The measurements were conducted using, 633nm of laser excitation source and 30 seconds of integration time on a DXR Raman Microscope. The Raman spectrum of acetaminophen shown in Figure 20, is dominated by peaks at 797, 855, 1136, 1323, 1561, 1605, and 1648cm^{-1}, which are attributed to CNC ring stretching, ring breathing, C–C ring stretching, amide III, amide II, ring stretching, and amide I modes, respectively.

These results are consistent with the reports in literature [135]. The acetaminophen detection proved that this capillary substrate does not only detect common Raman dye like R6g but can also detect other Raman active molecules.

3.3 PDMS device

The capillary SERS substrate has large hotspot density and high surface area, making it useful in detection of organic chemicals in liquid medium. But from a commercial point of view, the capabilities of this substrate need to be expanded. The formation of dendrites in the substrate is a random process, and so we do not know where the hotspots will be generated and how these dendrites are formed inside the capillary. With the capillary substrate characterization using SEM cannot be done without breaking the capillary tube. To surmount this limitation, we fabricated a device with channel in polydimethylsiloxane (PDMS) covered by a removable glass cover slip. Using this substrate, we can characterize dendrites using SEM without breaking the device. This PDMS device carries over all the advantages of the capillary substrate, as it has the same 3D silver dendrite nanostructure with high surface area and high hotspot density.

3.3.1 PDMS device fabrication

Polydimethylsiloxane (PDMS), also known as dimethylpolysiloxane or dimethicone is one of the common elastomers used in the market for a wide range of applications. PDMS belongs to a group of polymeric organosilicon compounds that are commonly referred to as silicones. PDMS has several useful material properties leading to its

application as molds for various purposes. It is chemically inert and provides a low interfacial free energy surface. It can be molded into any shape and is also optically transparent, nontoxic, with good gas permeability and thermal stability. Flexible microchannel devices in nanoscale engineering are mostly made with PDMS.

Rapid prototyping is a widely used method to develop molds for PDMS applications. 3D printing, which is a simple lithography technique can be used to make a master mold for the PDMS device. A mold of inner dimensions (40x10x5mm) with a small projection of 0.5mm at the center is fabricated in a 3D printer using Teflon as shown in Figure 21 (a). The PDMS used in this study is supplied in two components, a base, and a curing agent from the manufacturer. The reaction between vinyl groups in the base and silicon hydride groups in the curing agent causes the formation of a cross-linked elastomeric solid. The base and curing agent are mixed well in the ratio of 10:1 respectively, following manufacturer's instructions. This liquid pre-polymer is poured into the master mold and allowed to cure in air for a day, without disturbing. This is illustrated in Figure 21 (b). The setup can be placed in a vacuum chamber at an increased temperature to speed up the curing process and to remove air bubbles present inside the pre-polymer. The liquid PDMS pre-polymer conforms to the shape of the master mold and replicates the features of the mold with high compliance. The PDMS device with microchannel as shown in Figure 21 (c) can be released from the mold without damaging the mold or itself, because of the low surface free energy and the inherent elasticity properties of PDMS.

The surface of PDMS can be modified to reduce Raman signal interference by depositing thin films of various materials. The fabricated PDMS elastomeric device with a

micro channel at the center is coated with silver by a simple sputtering process. Around 100-150nm silver was deposited on the PDMS as shown in Figure 21 (d).

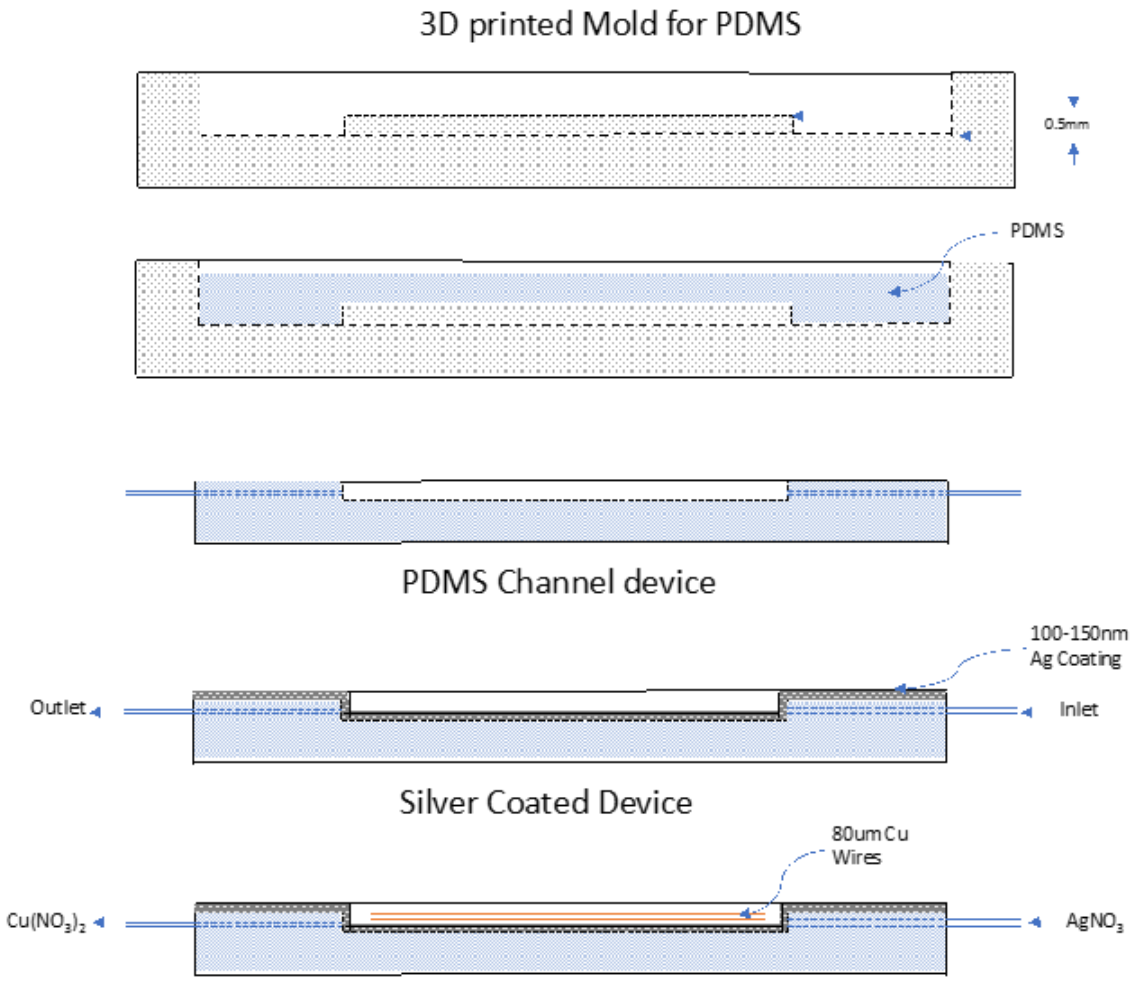

Figure 21: (a) 3D printed mold for PDMS. (b) Liquid pre-polymer PDMS is poured into the mold. (c) Elastomeric solid PDMS with one channel. (d) PDMS coated with silver. (e) Silver coated PDMS device with copper wire inside the channel

After depositing the PDMS with silver, copper wire of 20mm in length and diameter of 80µm is placed inside the channel. The copper wire is cleaned with acetone and

distilled water to remove any contaminants and dust, before placing it inside the PDMS channel shown in Figure 21 (e). Then the PDMS with the copper wire is placed in between two glass slides which are then pressed firmly using paper clips. This is done to avoid any leakage while injecting the solution into the PDMS channel. Now a small needle is used to pierce through the PDMS longitudinally from one side of the device, till it reaches the channel to provide an outlet for drainage.

3.3.2 Synthesis of dendrites inside PDMS microchannel

3ml of 0.1M $AgNO_3$ solution is made to flow into the PDMS setup containing the copper wire, for 10 minutes at a flowrate of 0.30ml/minute. The silver nitrate reacts with copper wire to form silver dendrite by the GRR process. The reduced silver grows in a preferential manner which leads to the formation of dendrites shown in Figure 22. The used solution containing reaction products ($Cu(NO_3)_2$) and byproducts is drained through the needle at the other side of the channel. After the dendrite formation, the channel is washed for several minutes with deionized water and air dried to remove any excess solution and reaction byproducts. Washing is done very carefully to prevent any damage to the formed silver dendrites.

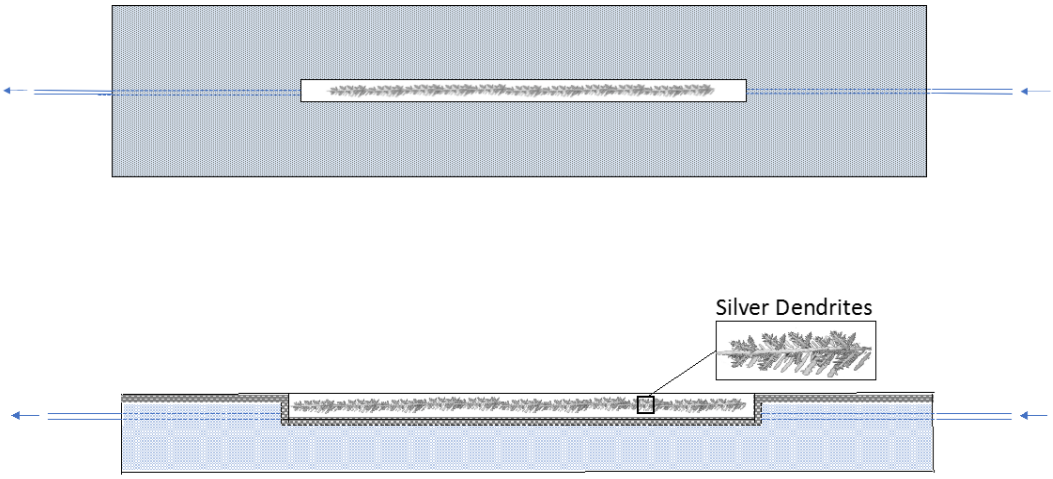

Figure 22: Silver dendrites formed inside PDMS channel

Depending upon our needs and requirement, multichannel SERS devices can also be fabricated. SERS device with two channels is shown in Figure 23. The channel length in the device can also be increased or decreased to convenience based on application. But at the same time, volume of the silver nitrate solution and its flowrate must be adjusted according to the length and diameter of the copper wire used.

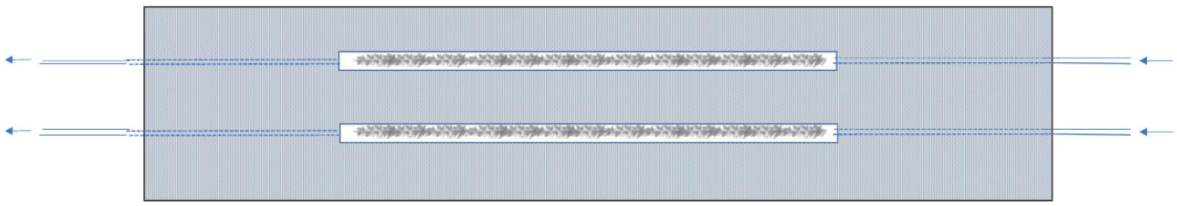

Figure 23: Two channel PDMS SERS device with silver dendrites

3.3.3 Characterization of silver dendrites in PDMS device

Field Emission Scanning Electron Microscope (FE-SEM, ZEISS Supra 55 VP) at 10 kV was used to study the dendritic structure of the silver. The SEM image from Figure 24 shows that the dendrites are very thick, such that the diameter of the main trunk is 4μm and the branch is 2μm approximately. This thick dendritic structure is obtained because of the reaction of copper wire with a large concentration of silver nitrate. The angle between the branch and the main trunk is measured to be 54.3 degrees. It is close to the theoretically calculated angle between (111) and (200) planes, which is 54.7 degrees.

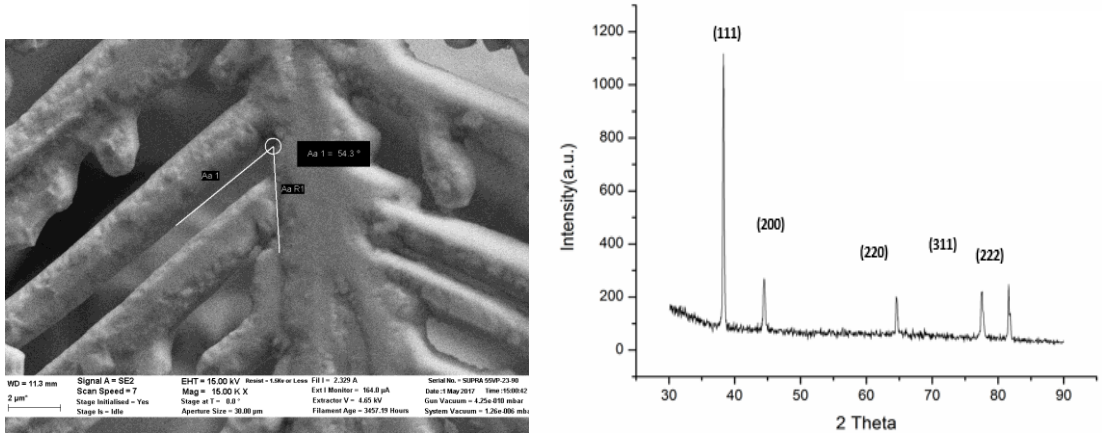

Figure 24: SEM image and XRD pattern of silver dendrites

X-ray powder diffraction is used to characterize the crystalline structure of the silver dendrite. X-ray diffraction is done with a Cu Kα source (Siemens D500). Scanning is done at the rate of 2° per minute at an angle from 20° to 90°. XRD pattern from Figure 24 shows that the diffraction peaks are seen at (111), (200), (220), (311) and (222) planes. This

diffraction planes belongs to the FCC crystal structure of silver dendrites. The crystallinity of silver dendrites can be noticed from the sharpness of the peaks.

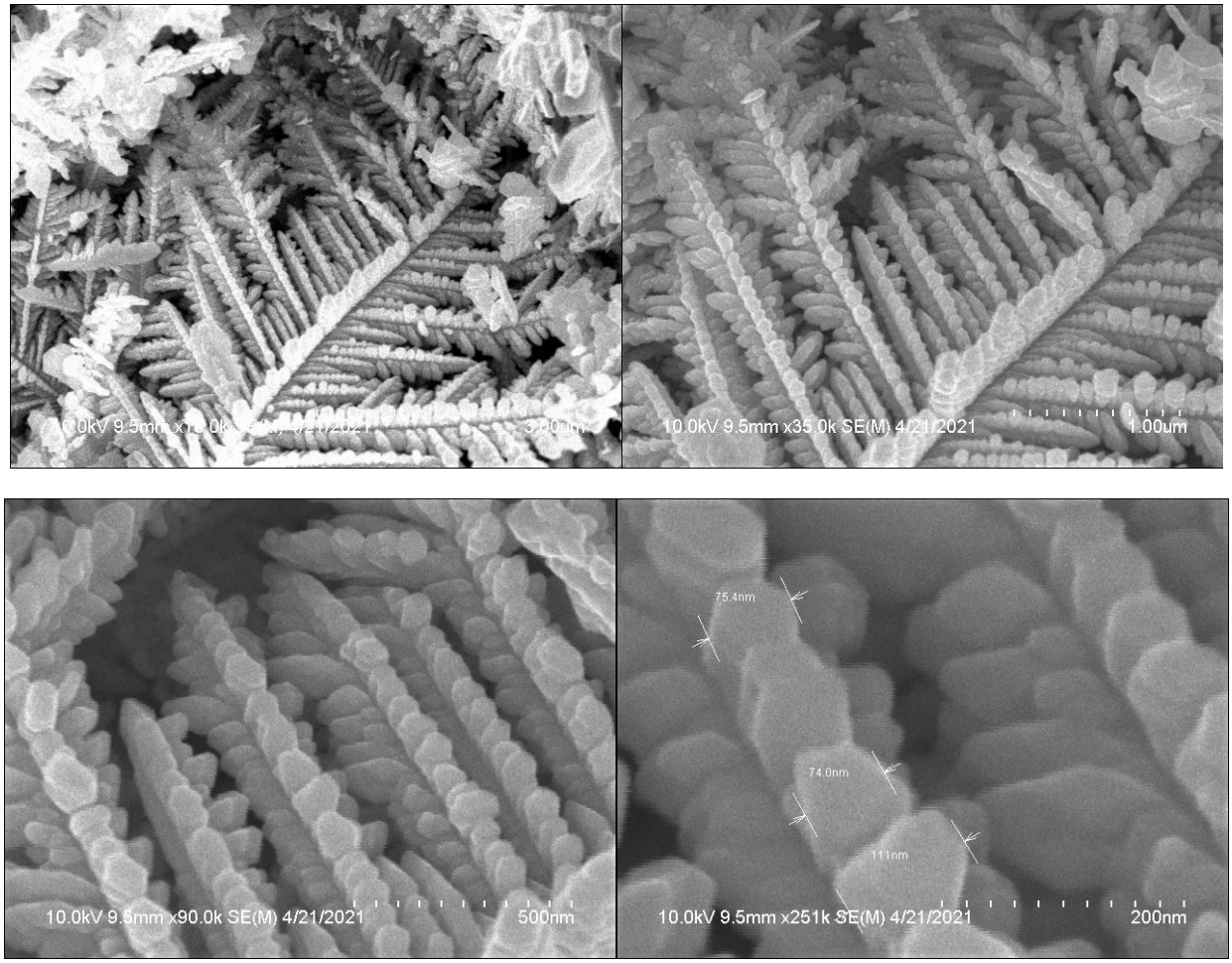

Figure 25: SEM images of silver dendrites in PDMS device at different magnifications

Figure 25 shows the SEM image of silver dendrite with different magnifications at x 10k, x 35k, x 90k and x 251k. The branch and trunk of the dendrites are approximately 50-200nm in diameter. The gaps between the dendrite branches are almost 1-30nm. When analyte molecules that are to be detected is near the tip of the dendrite or in the gap between these dendrite branches, the Raman signal of that molecule is enhanced.

3.3.4 SERS measurements for Rhodamine-6g using PDMS device

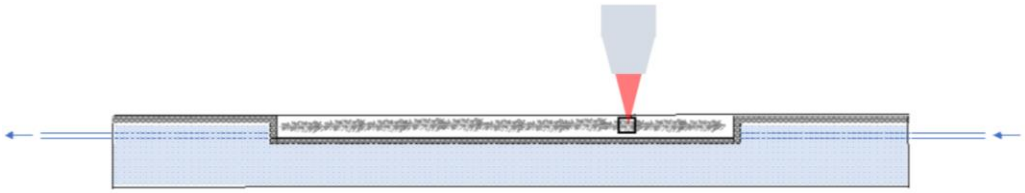

Figure 26: Schematic diagram of the device used for SERS measurement

Rhodamine-6g (R6g) is first used as an analyte molecule to test Raman enhancement in the PDMS device. R6g is diluted into an aqueous solution with concentrations ranging from 10^{-4} to 10^{-14} M. Each solution is detected independently. The prepared solution is injected into the PDMS channel using a syringe, till it reaches the other side of the channel. Raman Spectroscopy is conducted using DXR Thermo Fisher Raman microscope, with a 633nm He–Ne laser source with a power of 7W, a diffraction grating of 633 lines/mm, 10× objective lens and slit width of 50 cm^{-1}. The laser is focused on the dendrite as show in Figure 26 with an exposure time of 32s. Detection limit of the device while analyzing R6g was found to be 10^{-14} M. The characteristic Raman peaks for R6g molecules are 610, 767, 1184, 1360, 1510, 1570 and 1651cm^{-1}. These peaks correspond to the C-C-C ring in-plane vibrations, C-H out of plane bending, C-H in-plane bending vibrations, C-O-C stretching and C-C stretching of ring respectively [134].

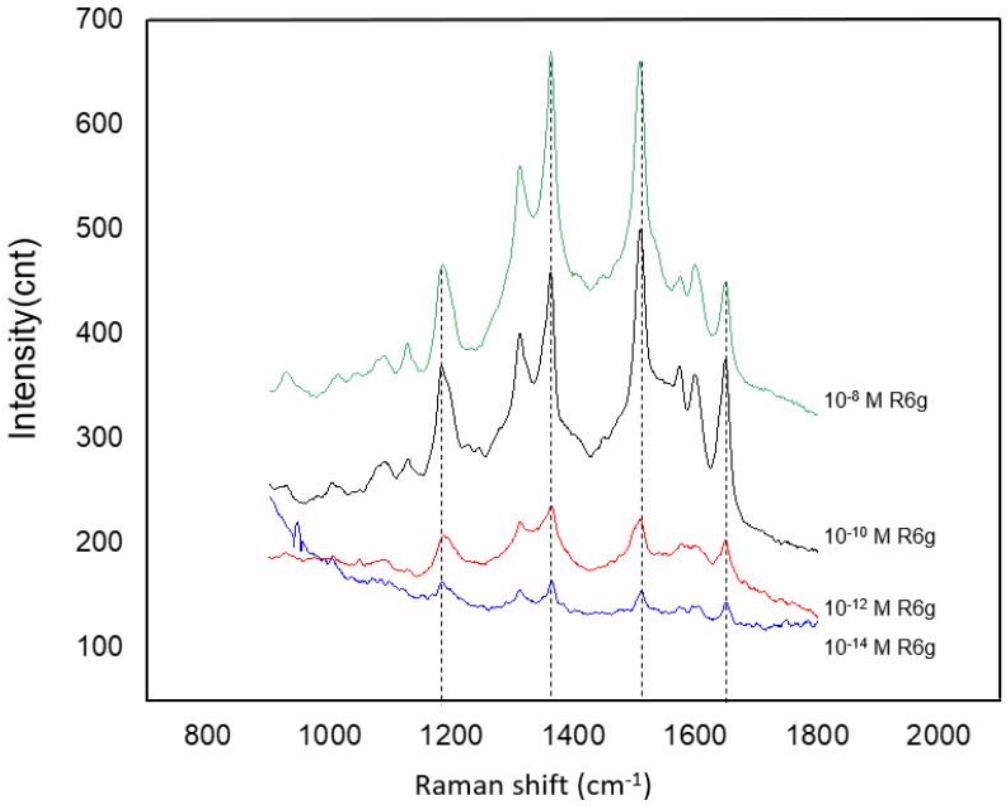

Figure 27: Raman spectrum for R6g in aqueous solution at lower concentrations using the PDMS device

3.4 FDTD simulation

As observed from Figure 27, concentrations as low as 10^{-14} M of R6g can be detected using the PDMS SERS device. To explain such low concentration detection, Finite Difference Time Domain (FDTD) simulation is performed using Lumerical FDTD software. FDTD simulation act as a Maxwell equation solver. It calculates the electric field around the dendritic structure from the incident electromagnetic wave. This simulation quantizes time and space into discrete steps. From the electric field obtained for different configurations of dendritic structure, enhancement factor is calculated.

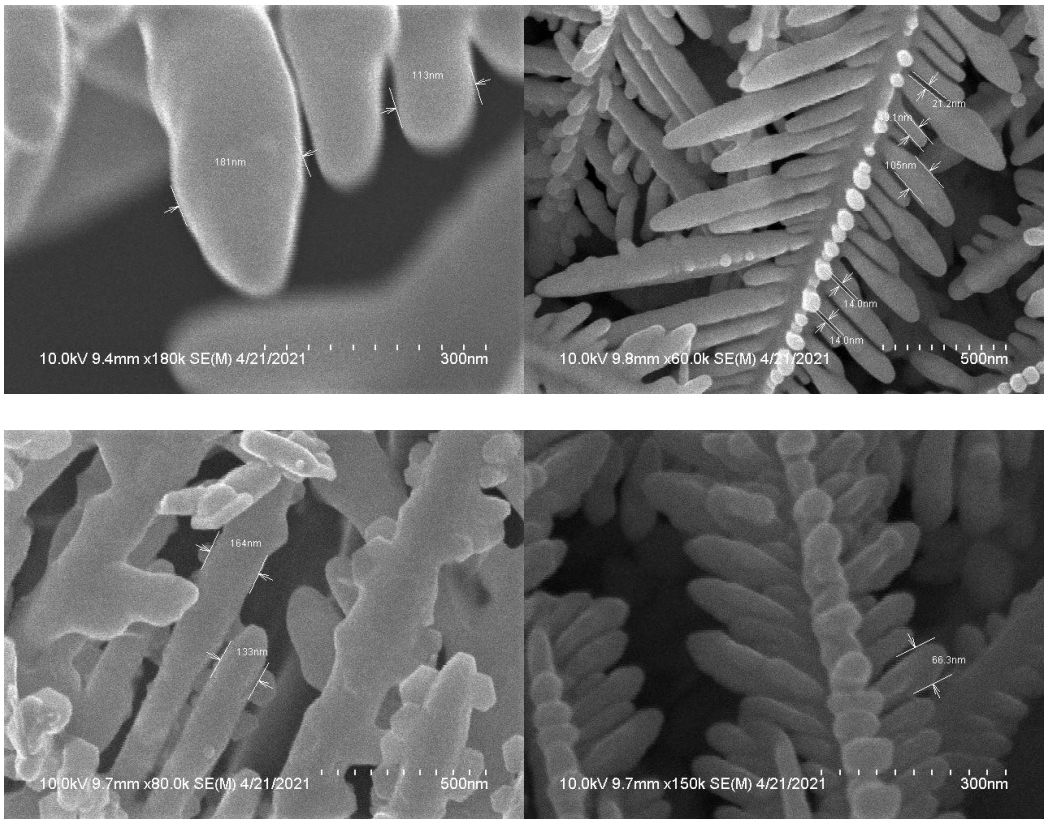

Figure 28: SEM images of the dendrites with diameter of their branches

Figure 28 shows the SEM images of the dendrites from the PDMS device that were used to obtain results for 10^{-14} M concentration of R6g. From Figure 25 and Figure 28 it is clear that the low concentration detection can be achieved if the dendritic branches are almost around 30 - 200nm in diameter and the gap between these branches are almost 1 - 50nm in distance. To make the 3D structure of the dendrites for using it in FDTD simulation, the diameter of the branch and the distance between the gap is averaged to be 100nm and 50nm, respectively. Upon simulating this structure, the maximum enhancement factor of this dendrite is calculated to be 10^6, which is observed in Figure 29 (a). The maximum enhancement is observed between the branches of the dendrites

rather than on the tips. Based on this observation, more simulations were conducted by maintaining the diameter of the branches to be a constant 100nm and varying only the gap between these branches. Simulations were performed with gap distances of 30nm and 10nm which are shown in Figure 29 (b) and (c) respectively. The results indicated that a maximum enhancement factor of 10^7 is obtained when the gap between the branches is reduced to 10nm. In light of these results, we conclude that a higher signal enhancement can be achieved if the gap distance between the dendrite branches is reduced.

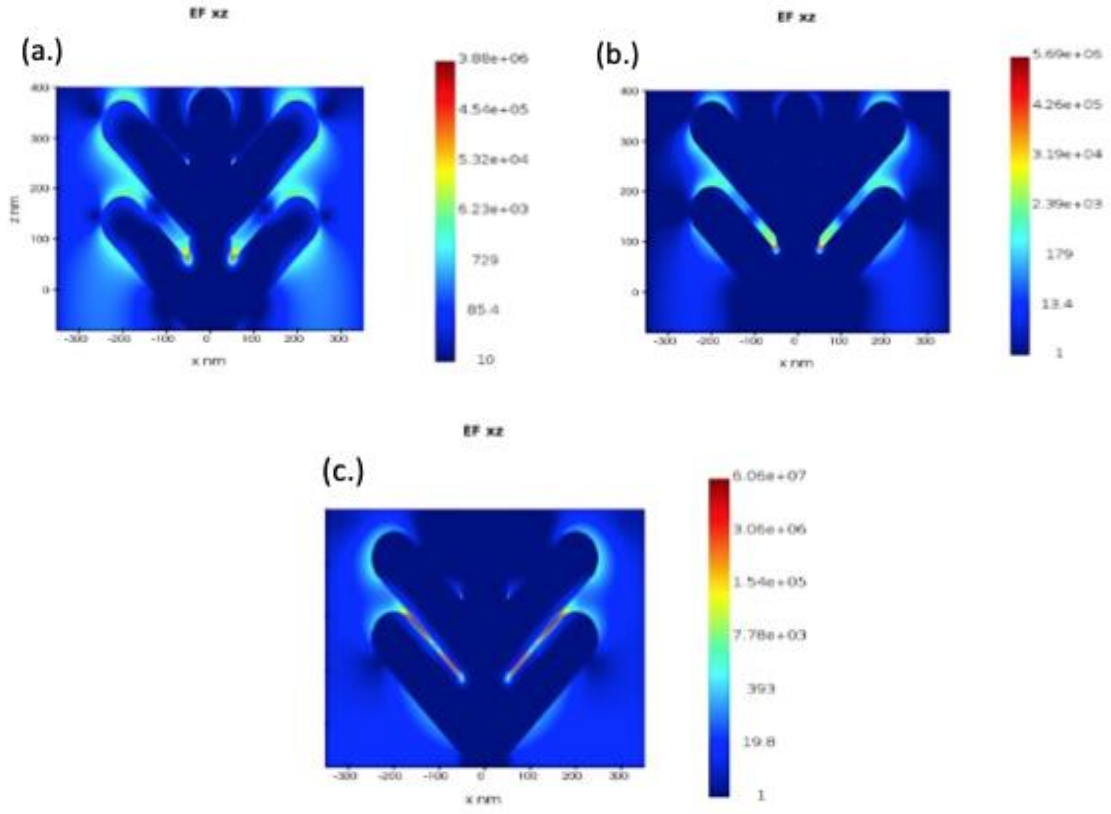

Figure 29: FDTD simulation of dendrite with a branch diameter of 100nm and gap between the branches at a distance of (a) 50nm, (b) 30nm, (c) 10nm

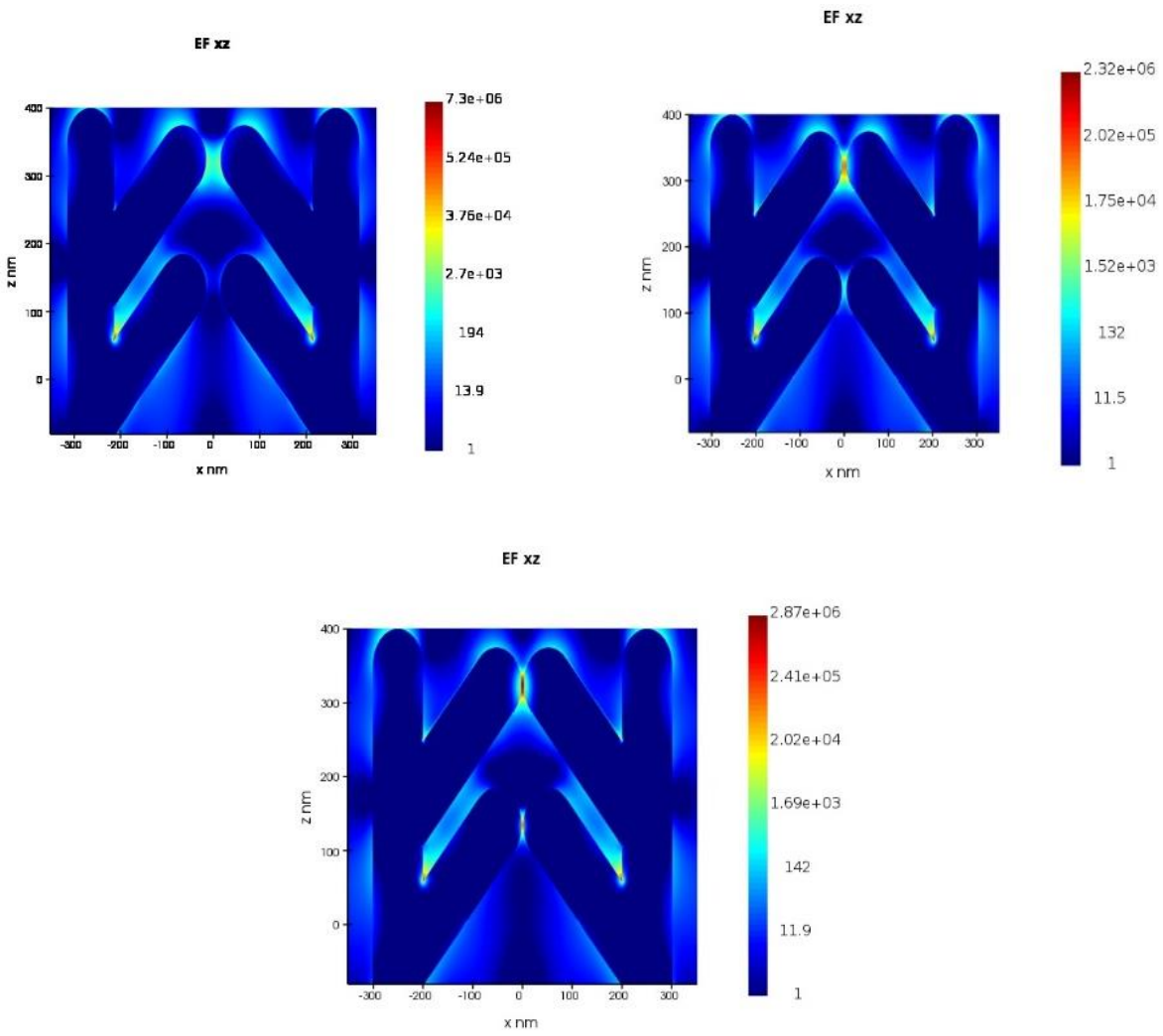

Figure 30: FDTD simulation of two dendrites with 100nm branch diameter and the gap between the tips of the branches at a distance of (a) 50nm, (b) 30nm, (c) 10nm

As the dendrite formation inside the PDMS channel is random, tips of multiple dendrites which themselves are hotspots, can be formed closer to one another and thereby interacting with each other creating stronger hotspots. In accordance with this assumption, simulations were conducted with two dendritic tips in close proximity. Three different distances of 50, 30 and 10nm between the dendrite tips were designed and the

results were analyzed. Figure 30 shows the simulation results under these conditions. Similar to the effect seen in the hotspots formed between dendrite branches, distance is inversely proportional to the enhancement factor between the dendrite tips. It was found that a maximum enhancement factor of 10^6 is obtained when the tips interact with each other at a 10nm distance. The overall enhancement in the structure is in the range of 10^6 - 10^7.

The ability to detect low concentrations could be due to the deposited silver on the PDMS surface. So R6g was detected using the device without any dendrites inside the channel. The resulting Raman spectrum showed no significant peaks even for 10^{-4} M concentration of R6g. This confirmed that the silver coating does not increase or affect the enhancement factor. Then we hypothesized that the hotspots could also be concentration point for the analyte molecules due to a filtering effect; when the analyte solution is passed into the channel the 3D silver dendrites act as a filter and trap the molecules in the hotspot. This increases the concentration of the molecule in the hotspot regions. This inherent ability of the device to trap the analytes greatly aids in the detection of low concentration molecules. We suspect that even lower concentrations can be detected if the solution is overflowed into the device for more than 30 seconds.

3.5 Calibrating the device using Rhodamine-6g

To detect any Raman active molecule in liquid solutions using the PDMS device, it must be made sure that the dendritic structure formed inside the channel of the PDMS device is intact and capable of enhancing Raman signal. To confirm the integrity of the

dendrites, a method to calibrate this device using a reference molecule is established. R6g is chosen to be used as the reference molecule. Based on the observations from Figure 27, as low as 10^{-14} M R6g solution concentration could be accurately detected. Hence, 10^{-12} M R6g concentration is chosen as a reference, to calibrate the device by obtaining a Raman spectrum. After a clear Raman spectrum with well-defined peaks is obtained from this solution, the integrity of the dendritic structure and the hotspot locations inside the device are confirmed. Thus, it can be established that the device is accurate and sensitive enough to detect any Raman active molecule in solution. After calibrating the device, the channel is thoroughly washed using deionized water carefully, to remove any and all R6g present. Water is passed into the device channel slowly without disturbing the dendrites, for approximately 10 minutes and then air dried. This washing process is essential to avoid any Raman signal interference from R6g molecules. Now, the device is calibrated and ready to be used to detect Raman active molecules in liquid solution.

3.5.1 SERS measurements using the R6g-calibrated PDMS devices

Methylene blue:

Using the calibrated device, as low as 10^{-10} M Methylene blue in aqueous solution is detected, in Figure 31 shows characteristic Raman peaks at 889, 1033, 1149 cm^{-1}, all of which correspond to in-plane bending of C–H and 1301, 1394, 1498 and 1623cm^{-1}, which correspond to in-plane ring deformation of C–H, symmetrical stretching of C–N, asymmetrical stretching of C–N, ring stretching of C–C, respectively [136].

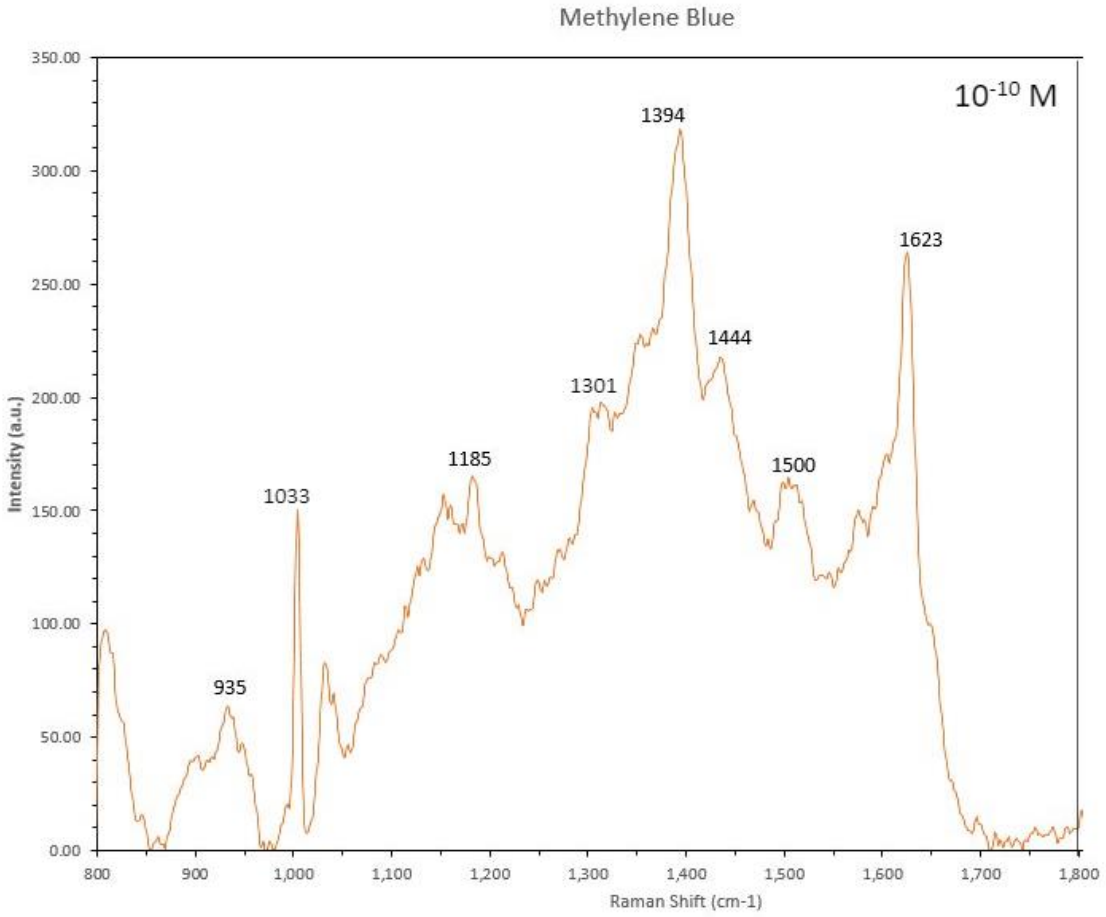

Figure 31: Raman spectrum of 10^{-10} M concentration of Methylene blue

4-Mercaptobenzoic acid (4MBA):

The calibrated device is also used to detect another Raman active molecule 4MBA in aqueous solution. Concentration as low as 10^{-5} M is detected. Figure 32 shows major vibrational modes at 1014, 1075, 1139, 1186, 1386, 1587 cm-1, which correspond to stretching of C-C ring-breathing modes (~1070 and 1575 cm^{-1}), other less intense modes including bending of C-H (1132 and 1173 cm-1) and vs (COO-) (1375 cm-1) [137].

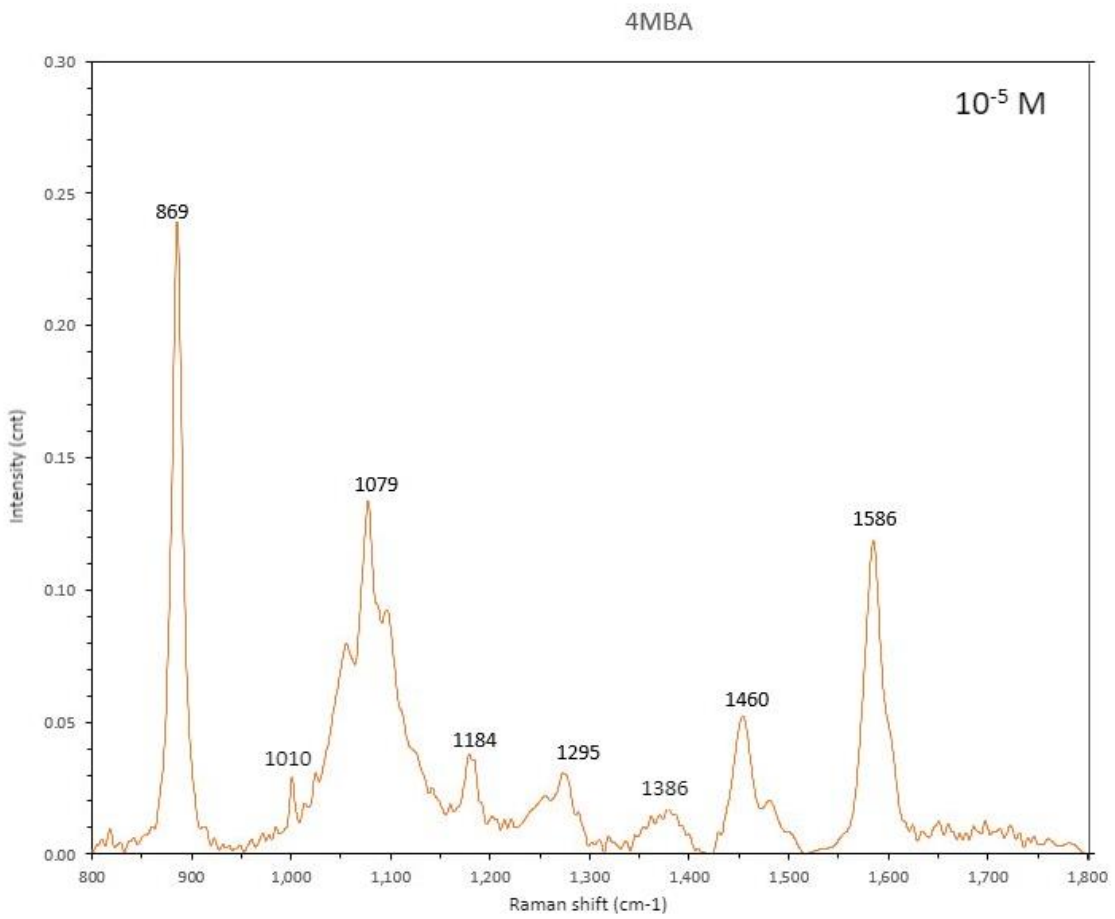

Figure 32: Raman spectrum of 10^{-5} M concentration of 4-Mercapitobenzoic acid

Thiabendazole (TBZ):

In view of practical applications, using the PDMS SERS device we detected Thiabendazole (TBZ) molecules in liquid solution. TBZ is a commonly used pesticide in apple and orange farming that prevents diseases like Downey mildew, Black rot, etc. This chemical can pose a serious hazard to human health upon ingestion. TBZ is insoluble in water, so methanol is used to make a liquid solution of TBZ. Using the calibrated device, as low as 0.0005 g/L (0.5 ppm) TBZ dissolved in methanol is detected. The spectrum

depicted in Figure 33 is obtained after removing the major Raman peaks for methanol (at 1030 and 1460cm^{-1}). The major peaks of TBZ are seen at 643, 779, 1011, 1276, 1454, 1577cm^{-1}. These are assigned to the stretching and bending of C-S-C and C-H in ring 1 and C-C in ring 3; S-C and in-plane bending of C=N in ring 1; stretching of C-N in ring 2 and stretching of C-C in ring 2 and 3; stretching of C-C in ring 1 and stretching of C-N in ring 2; bending of C-H in ring 1; and C-C stretching and N=C stretching in ring 2; C=C and C-C stretching in ring 3; C-H and C-N-H bending in ring 2 respectively [138].

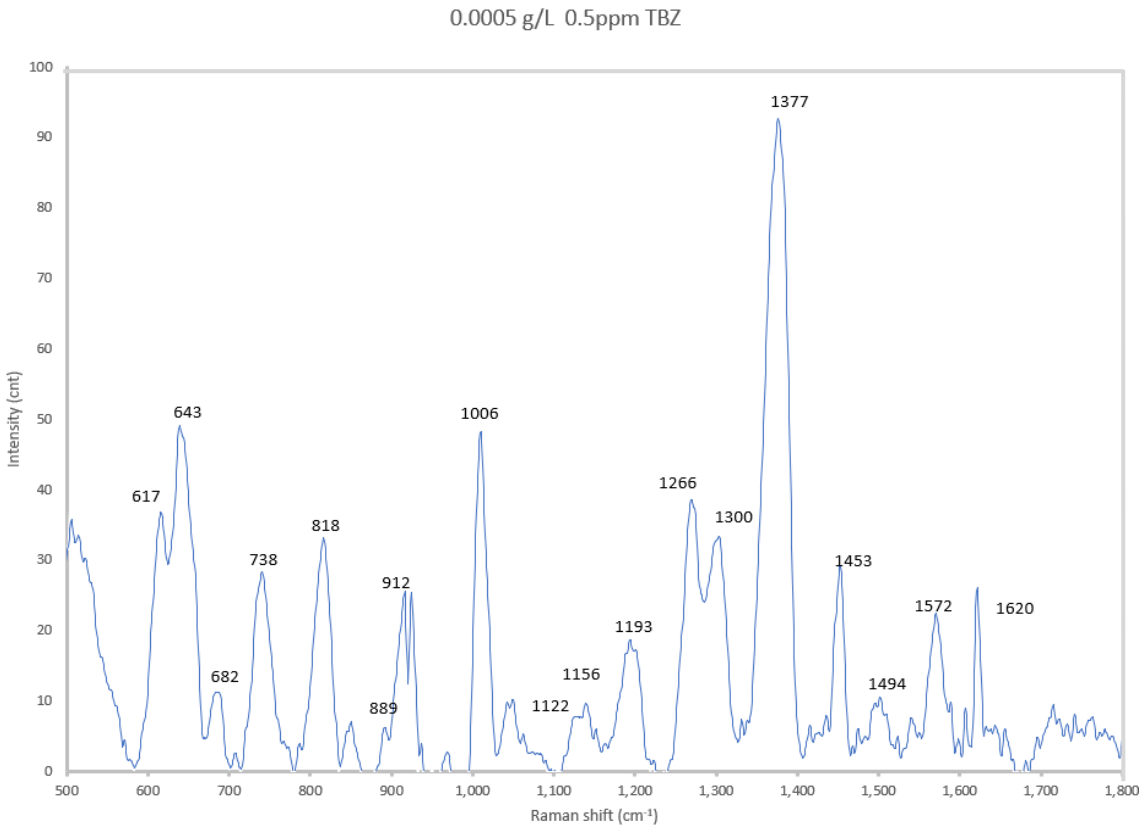

Figure 33: Raman spectrum of 0.5 ppm of Thiabendazole

Chapter 4

Conclusion

An innovative design was made to develop hierarchical Ag nano dendrites inside the channels of a PDMS device. A simple synthesis process was employed to create these nanostructures. Such device can be used as SERS substrate to detect organic chemicals in liquid solutions without much of sample preparation. The Ag nano dendrites provide large surface area with high density hotspots along all three dimensions, which leads to a strong enhancement of Raman signal from the molecules adsorbed on to their surface. Detection of 10^{-14} M concentration of R6g in aqueous solution was achieved using this device. Low concentrations of organic chemicals such as 4- Mercaptobenzoic acid, Methylene blue, and Thiabendazole in liquid solutions were also detected using this device.

The fabrication process of this device is very simple. 3D Ag nano dendrites were synthesized by a Galvanic Replacement Reaction (GRR) between copper wire inside the PDMS channel and 0.1M silver nitrate solution injected into the channel at a specific flowrate of 0.30ml/min. The dendritic structure was verified by SEM and XRD. FDTD simulation was conducted to study the enhancement mechanism near the surface of the dendrites for various branch sizes and gap distances. Aiming for real world applications, the device was calibrated with 10^{-12} M R6g to ensure a reliable detection. The calibrated device was tested to detect molecules of 4-MBA, Methylene blue and Thiabendazole in

liquid solutions, showing chemicals in flowing liquid medium can be detected and/or monitored with high sensitivity and reproducibility.

Reference

1. R. M. Black, R. J. Clarke, R. W. Read, M. T. Application of gas chromatography-mass chromatography to analysis chemical wafer sample. Journal of Chromatography. 662, 301 (1994)

2. G. A. Sega, B. A. Tomkins, W. H. Griest. Analysis of methylphosphonic acid, ethyl methylphosphonic acid and isopropyl methylphosphonic acid at low microgram per liter levels in groundwater. Journal of Chromatography. A. 1997 Nov 28;790(1-2):143-52.

3. S. A. Oehrle, P. C. Bossle. Analysis of nerve agent degradation products using capillary ion electrophoresis. Journal of Chromatography. A Volume 692, Issues 1–2, 10 February 1995, Pages 247-252

4. Q. Liu, X. Hu, J. Xie. Determination of nerve agent degradation products in environmental samples by liquid chromatography–time-of-flight mass spectrometry with electrospray ionization. Analytica Chimica Acta 512, 93 (2004)

5. William R. Creasy. Post column derivatization liquid chromatography/mass spectrometry for detection of chemical-weapons-related compounds. Journal of the American Society for Mass Spectrometry volume 10, pages440–447(1999)

6. G. A. Eiceman, Z. Caras: Ion Mobility Spectrometry. CRC Press. Published November 16, 2016

7. N. Krylova, E. Krylov, G. A. Eiceman. Field Dependence of Mobilities for Gas-Phase-Protonated Monomers and Proton-Bound Dimers of Ketones by Planar Field Asymmetric Waveform Ion Mobility Spectrometer (PFAIMS). Journal of Physical Chemistry A 2002, 106, 22, 5437–5444

8. L. D. Hoffland, R. J. Piffath, J. B. Bouck. Spectral Signatures of Chemical Agents and Simulants. Optical Engineering. 24(6), 982 (1985)

9. E. H. J. Braue, M. G. Pannella. CIRCLE CELL FT-IR Analysis of Chemical Warfare Agents in Aqueous Solutions. Applied Spectroscopy. 44, 1513 (1990)

10. C. H. Tseng, C. K. Mann, T. J. Vickers. Determination of organics on metal surface by Raman spectroscopy. Applied Spectroscopy. 47, 1767 (1993)

11. S. Kanan, C. Tripp. An infrared study of organophosphonates on silica: a prefiltering strategy for the detection of nerve agents on metal oxide sensors, Langmuir 17, 2213 (2001)

12. S. D. Christesen. Raman cross sections of chemical agents and simulants. Applied Spectroscopy. 42, 318 (1988)

13. S. Christesen, B. Maciver, L. Procell, D. Sorrick, M. Carrabba, J. Bello. Nonintrusive Analysis of Chemical Agent Identification Sets Using a Portable Fiber-Optic Raman Spectrometer. Applied Spectroscopy. 53-7, 850 (1999)

14. D. L. Jeanmaire, R. P. Van Duyne. Surface Raman Spectro electrochemistry: Part I. Heterocyclic, aromatic, and aliphatic amines adsorbed on the anodized silver electrode. Journal of Electroanalytical Chemistry and Interfacial Electrochemistry. 84, 1 (1977)

15. Schlücker S. Surface-enhanced Raman spectroscopy: concepts and chemical applications. Angewandte Chemie (International ed. in English). 2014 May;53(19):4756-4795.

16. Yu, J. and X. Zhou, Synthesis of Dendritic Silver Nanoparticles and Their Applications as SERS Substrates. Advances in Materials Science and Engineering, 2013. 2013: p. 1-4.

17. Kneipp, K., Wang, Y., Kneipp, H., Perelman, L. T., Itzkan, I., Dasari, R. R., & Feld, M. S. (1997). Single molecule detection using surface-enhanced Raman scattering (SERS). Physical review letters, 78(9), 1667.

18. Nie, S., & Emory, S. R. (1997). Probing single molecules and single nanoparticles by surface-enhanced Raman scattering. science, 275(5303), 1102-1106.

19. Wang, H. H., Liu, C. Y., Wu, S. B., Liu, N. W., Peng, C. Y., Chan, T. H., ... & Wang, Y. L. (2006). Highly Raman-enhancing substrates based on silver nanoparticle arrays with tunable sub-10 nm gaps. Advanced Materials, 18(4), 491-495.

20. Dieringer, J. A., Lettan, R. B., Scheidt, K. A., & Van Duyne, R. P. (2007). A frequency domain existence proof of single-molecule surface-enhanced Raman spectroscopy. Journal of the American Chemical Society, 129(51), 16249-16256.

21. Grabar, K. C., Freeman, R. G., Hommer, M. B., & Natan, M. J. (1995). Preparation and characterization of Au colloid monolayers. Analytical chemistry, 67(4), 735-743.

22. Rivas, L., Sanchez-Cortes, S., Garcia-Ramos, J. V., & Morcillo, G. (2000). Mixed silver/gold colloids: a study of their formation, morphology, and surface-enhanced Raman activity. Langmuir, 16(25), 9722-9728.

23. Reiner EJ, Clement RE, Okey AB, Marvin CH (2006) Advances in analytical techniques for polychlorinated dibenzo-p-dioxins, polychlorinated dibenzofurans, and dioxin-like PCBs. Analytical Bioanalytical Chemistry 386(4):791–806

24. Pushkarsky, M. B., Dunayevskiy, I. G., Prasanna, M., Tsekoun, A. G., Go, R., & Patel, C. K. N. (2006). High-sensitivity detection of TNT. Proceedings of the National Academy of Sciences, 103(52), 19630-19634

25. Baker, B. R., Lai, R. Y., Wood, M. S., Doctor, E. H., Heeger, A. J., & Plaxco, K. W. (2006). An electronic, aptamer-based small-molecule sensor for the rapid, label-free detection of cocaine in adulterated samples and biological fluids. Journal of the American Chemical Society, 128(10), 3138-3139.

26. Squires, T. M., Messinger, R. J., & Manalis, S. R. (2008). Making it stick convection, reaction, and diffusion in surface-based biosensors. Nature biotechnology, 26(4), 417.

27. Fang Y, Seong N-H, Dlott DD (2008) Measurement of the distribution of site enhancements in surface-enhanced Raman scattering. Science 321(5887):388–392

28. Michaels AM, Jiang, Brus L (2000) Ag nanocrystal junctions as the site for surface-enhanced Raman scattering of single Rhodamine 6G molecules. Journal of Physical Chemistry B 104(50):11965–11971

29. Bosnick KA, Jiang, Brus LE (2002) Fluctuations and local symmetry in single-molecule Rhodamine 6G Raman scattering on Ag nanocrystal aggregates. Journal of Physical Chemistry B 106(33):8096–8099

30. Dieringer JA, Lettan RB 2nd, Scheidt KA, Van Duyne RP (2007) A frequency domain existence proof of single-molecule surface-enhanced Raman spectroscopy.

31. A. M. Alak, T. Vo-Dinh. Surface-enhanced Raman spectrometry of organophosphorus chemical agents. Analytical Chemistry 59, 2149 (1987).

32. K. M. Spencer, J. Sylvia, S. Clauson, J. Janni: Proc. SPIE 4577, 158 (2001)

33. S. D. Christesen, M. J. Lochner, M. Ellzy, K. M. Spencer, J. Sylvia, S. Clauson: 23rd Army Science Conference (ASC, Orlando, FL 2002)

34. P. Tessier, S. Christesen, K. Ong, E. Clemente, A. Lenhoff, E. Kaler, O. Velev. On-line spectroscopic characterization of sodium cyanide with nanostructured gold SERS substrates. Applied Spectroscopy. 56, 1524 (2002)

35. S. Farquharson, P. Maksymiuk. Simultaneous Chemical Separation and Surface-Enhanced Raman Spectral Detection Using Silver-Doped Sol-Gels. Applied Spectroscopy 57, 479 (2003)

36. Tian, L., Su, M., Yu, F. et al. Liquid-state quantitative SERS analyzer on self-ordered metal liquid-like plasmonic arrays. Natures Communication 9, 3642 (2018).

37. Fei Chan, Y., Xing Zhang, C., Long Wu, Z., Mei Zhao, D., Wang, W., Jun Xu, H., & Sun, X. M. (2013). Ag dendritic nanostructures as ultra-stable substrates for surface-enhanced Raman scattering. Applied Physics Letters, 102(18), 183118.

38. Shahab Ranjbar Bahadori, Linyu Mei, Aseem Athavale, Yu-jen Chiu, Christopher S. Pickering, and Yaowu Hao. New Insight into Single-Crystal Silver Dendrite Formation and Growth Mechanisms. Crystal Growth & Design 2020 20 (11), 7291-7299.

39. A. Weber (Editor). Raman Spectroscopy of Gases and Liquids. Topics in Current Physics. John Springer-Verlag, Berlin, 1979.

40. Derek A. Long. The Raman Effect. John Wiley & Sons, New York, 2002.

41. Hahn, D. W. (2007). Raman scattering theory. Department of Mechanical and Aerospace Engineering, University of Florida.

42. N.B. Colthup, L.H. Daly, S.E. Wiberley. Introduction to Infrared and Raman Spectroscopy. (Third Edition) Academic Press, 1990.

43. Leng, Yang. Vibrational Spectroscopy for Molecular Analysis. Singapore; Hoboken, NJ:: J Wiley,, 2008. Web.

44. M. Fleischman, P. J. Hendra, A. J. McQuillan. Raman spectra of pyridine adsorbed at a silver electrode. Chemical Physics Letter 26, 123 (1974)

45. D. L. Jeanmaire, R. P. Van Duyne. Surface Raman Spectro electrochemistry. Part I. Heterocyclic, aromatic, and aliphatic amines adsorbed on the anodized silver electrode Journal of Electroanalytical Chemistry 84, 1 (1977)

46. M. G. Albrecht, J. A. Creighton. Anomalously intense Raman spectra of pyridine at a silver electrode. Journal of the American Chemical Society 99, 5215 (1977)

47. K. Kneipp, M. Moskovits and H. Kneipp. Surface-enhanced Raman Scattering-Physics and Applications, Topics in Applied Physics. 103 2006

48. Moskovits, M. (1978). Surface roughness and the enhanced intensity of Raman scattering by molecules adsorbed on metals. The Journal of Chemical Physics, 69(9), 4159-4161

49. M. A. Paesler, P. J. Moyer: Near-Field Optics: Theory, Instrumentation and Applications (Wiley, New York 1996)

50. N. Halas (Ed.): Plasmonics: Metallic Nanostructures and Their Optical Properties (SPIE 2003)

51. J. D. Jackson. Electromagnetic Theory. 3rd edition Wiley, New York (1998)

52. E. J. Zeman, G. C. Schatz. An accurate electromagnetic theory study of surface enhancement factors for silver, gold, copper, lithium, sodium, aluminum, gallium, indium, zinc, and cadmium. The Journal of Physical Chemistry. 91(3), 634 (1987)

53. M. Kerker, D. S. Wang, H. Chew. Surface enhanced Raman scattering (SERS) by molecules adsorbed at spherical particles. Applied Optics 19(19), 3373 (1980)

54. G. C. Schatz. Theoretical studies of surface enhanced Raman scattering. Accounts of Chemical Research 17(10), 370 (1984)

55. H. Metiu, P. Das. The Electromagnetic Theory of Surface Enhanced Spectroscopy. Annual Review of Physical Chemistry 35, 507 (1984)

56. H. Xu, J. Aizpurua, M. Kall, P. Apell. Electromagnetic contributions to single-molecule sensitivity in surface-enhanced Raman scattering. Physical Review E 62, 4318 (2000)

57. G. C. Schatz, R. P. Van Duyne. Electromagnetic Mechanism of Surface-enhanced Spectroscopy. Handbook of Vibrational Spectroscopy, vol. 1 759 Wiley, New York (2002)

58. Jensen, L., Aikens, C. M., & Schatz, G. C. Electronic structure methods for studying surface-enhanced Raman scattering. Chemical Society Reviews, 37(5), 1061-1073 (2008)

59. W.H. Yang, J. Hulteen, G. C. Schatz, R. P. Van Duyne. A surface-enhanced hyper-Raman and surface-enhanced Raman scattering study of trans-1,2-bis(4-pyridyl)ethylene adsorbed onto silver film over nanosphere electrodes. Vibrational assignments: Experiment and theory. The Journal of Chemical Physics 104, 4313 (1996)

60. T. Iliescu, M. Baia, I. Pavel. Raman and SERS investigations of potassium benzylpenicillin. Journal of Raman Spectroscopy. 37, 318 (2006)

61. T. Tanaka, A. Nakajima, A. Watanabe, T. Ohno, Y. Ozaki. Surface-enhanced Raman scattering of pyridine and p-nitrophenol studied by density functional theory calculations. Vibrational Spectroscopy. 34(1), 157 (2004)

62. T. Tanaka, A. Nakajima, A. Watanabe, T. Ohno, Y. Ozaki. Surface-enhanced Raman scattering spectroscopy and density functional theory calculation studies on adsorption of o-, m-, and p-nitroaniline on silver and gold colloid. Journal of Molecular Structure 661–662, 437 (2003)

63. S. D. Silaghi, G. Salvan, M. Friedrich, T. U. Kampen, R. Scholz, D. R. T. Zahn. Interface properties of metal/cytosine/Si (1 1 1):H heterostructures studied by means of SERS and DFT. Applied Surface Science 235(1-2), 73 (2004)

64. T. Iliescu, M. Bolboaca, R. Pacurariu, D. Maniu, W. Kiefer. Raman spectroscopy, surface-enhanced Raman spectroscopy and density functional theory studies of 2-formylfuran. Journal of Raman Spectroscopy. 34(9), 705 (2003)

65. K. L. Kelly, E. Coronado, L. Zhao, G. C. Schatz. The optical properties of metal nanoparticles: The influence of size, shape, and dielectric environment. Journal of Physical Chemistry B 107(3), 668 (2003)

66. Pilot R, Signorini R, Durante C, Orian L, Bhamidipati M, Fabris L. A Review on Surface-Enhanced Raman Scattering. Biosensors (Basel). 9(2) (2019)

67. E. Hao, G. C. Schatz. Electromagnetic fields around silver nanoparticles and dimers. The Journal of Chemical Physics. 120, 357 (2004)

68. L. Yin, V. K. Vlasko-Vlasov, A. Rydh, J. Pearson, U. Welp, S.-H. Chang, S. K. Gray, G. C. Schatz, D. E. Brown, C. W. Kimball. Surface plasmons at single nanoholes in

Au films. Applied Physics Letters 85, 467 (2004) Los Alamos National Laboratory, Preprint Archive

69. S. Nie, S. R. Emory. Probing Single Molecules and Single Nanoparticles by Surface-Enhanced Raman Scattering Science 275(5303), 1102 (1997)

70. K. Kneipp, Y. Wang, H. Kneipp, L. T. Perelman, I. Etzkan, R. R. Dasari, M. S. Feld. Single Molecule Detection Using Surface-Enhanced Raman Scattering (SERS). Physical Review Letters 78, 1667 (1977)

71. H. Xu, E. J. Bjerneld, M. Kall, L. Borjesson. Spectroscopy of Single Hemoglobin Molecules by Surface Enhanced Raman Scattering. Physical Review Letters 83, 4357 (1999)

72. Le Ru E.C., Etchegoin P.G. Principles of Surface Enhanced Raman Spectroscopy. Elsevier; Amsterdam, The Netherlands: 2009.

73. U. Kreibig, C. Von Frags. The limitation of electron mean free path in small silver particles. Zeitschrift für Physik 224(4), 307 (1969)

74. Kreibig, U., & Zacharias, P. Surface plasma resonances in small spherical silver and gold particles. Zeitschrift für Physik, 231(2), 128-143 (1970)

75. Dignam, M. J., & Moskovits, M. Optical properties of sub-monolayer molecular films. Journal of the Chemical Society, Faraday Transactions 2: Molecular and Chemical Physics, 69, 56-64 (1973)

76. W.-H. Yang, G. C. Schatz, R. P. Van Duyne. Discrete dipole approximation for calculating extinction and Raman intensities for small particles with arbitrary shapes. The Journal Chemical Physics. 103, 869 (1995)

77. A. Taflove, S. C. Hagness. The Finite-Difference Time-Domain Method. Artech House Inc., Norwood, MA. (2005)

78. Song-Yuan Ding, Jun Yi, Jian-Feng Li, Bin Ren, De-Yin Wu, Rajapandiyan Panneerselvam & Zhong-Qun Tian. Nanostructure-based plasmon-enhanced Raman spectroscopy for surface analysis of materials. Nature Reviews Material 1, 16021 (2016).

79. Lianming Tong, Hongxing Xu & Mikael Käll. Nanogaps for SERS applications. Materials Research Bulletin 39, 163–168 (2014).

80. Huang Y, Zhou Q, Hou M, Ma L, Zhang Z. Nanogap effects on near- and far-field plasmonic behaviors of metallic nanoparticle dimers. Physical Chemistry Chemical Physics. 17(43):29293-8. (2015)

81. Pilot R., Signorini R., Fabris L. Surface-Enhanced Raman spectroscopy: Principles, Substrates, and Applications. In: Deepak F.L., editor. Metal

Nanoparticles and Clusters: Advances in Synthesis, Properties and Applications. 89–164. Springer International Publishing. (2018)

82. Hajisalem G, Nezami MS, Gordon R. Probing the quantum tunneling limit of plasmonic enhancement by third harmonic generation. Nano Letters. 14(11):6651-6654. (2014)

83. Md Jani, A. M.; Losic, D.; Voelcker, N. H. Nanoporous Anodic Aluminum Oxide: Advances in Surface Engineering and Emerging Applications. Progress in Material Science. 58, 636– 704. (2013)

84. Makaryan, T.; Esconjauregui, S.; Gonçalves, M.; Yang, J.; Sugime, H.; Nille, D.; Renganathan, P. R.; Goldberg-Oppenheimer, P.; Robertson, J. Hybrids of Carbon Nanotube Forests and Gold Nanoparticles for Improved Surface Plasmon Manipulation ACS Applied Material Interfaces. 6, 5344– 5349. (2014)

85. Chen, J.; Yang, L. Synthesis and SERS Performance of a Recyclable SERS Substrate Based on Ag NPs Coated TiO2 NT Arrays. Integrated Ferroelectrics. 1, 17– 23. (2013)

86. Liu, K.; Li, D.; Li, R.; Wang, Q.; Pan, S.; Peng, W.; Chen, M. Silver-Decorated ZnO Hexagonal Nanoplate Arrays as SERS-Active Substrates: An Experimental and Simulation Study. Journal of Material Research. 28, 3374– 3383. (2013)

87. Lo Faro, M.J.; D'Andrea, C.; Leonardi, A.A.; Morganti, D.; Irrera, A.; Fazio, B. Fractal Silver Dendrites as 3D SERS Platform for Highly Sensitive Detection of Biomolecules in Hydration Conditions. Nanomaterials. 9, 1630. (2019)

88. Bian, J.C., Shu. S, Li. J, Huang. C, Li. Y, Zhang. R. Reproducible, and recyclable SERS substrates: Flower-like Ag structures with concave surfaces formed by electrodeposition. Applied Surface Science. 333. 126-133. (2015)

89. Fang, J., Hahn, H., Krupke, R., Schramm, F., Scherer, T., Ding, B., & Song, X. Silver nanowires growth via branch fragmentation of electrochemically grown silver dendrites. Chemical Communications. (9), 1130-1132. (2009).

90. Zhang, J. H., Liu, H. Y., Zhan, P., Wang, Z. L., & Ming, N. B. Controlling the growth and assembly of silver nanoprisms. Advanced Functional Materials. 17(9), 1558-1566. (2007).

91. Liang, H., Li, Z., Wang, W., Wu, Y., & Xu, H. Highly Surface-roughened "Flower-like" Silver Nanoparticles for Extremely Sensitive Substrates of Surface-enhanced Raman Scattering. Advanced Materials. 21(45), 4614-4618. (2009).

92. Zhu, C., Meng, G., Huang, Q., Zhang, Z., Xu, Q., Liu, G., ... & Chu, Z. Ag nanosheet-assembled micro-hemispheres as effective SERS substrates. Chemical Communications. 47(9), 2709-2711. (2011).

93. Cheng, Z. Q., Nan, F., Yang, D. J., Zhong, Y. T., Ma, L., Hao, Z. H., ... & Wang, Q. Q. Plasmonic nanorod arrays of a two-segment dimer and a coaxial cable with 1 nm gap for large field confinement and enhancement. Nanoscale. 7(4), 1463-1470. (2015).

94. Zuzana Orságová Králová, Andrej Oriňak, Renáta Oriňaková, Ondrej Petruš, Ján Macko, Jozef Radoňak, Lucia Sukovská Lakyová, Zuzana Jurašeková, Roger M. Smith, Magdaléna Strečková, Karol Koval. Electrochemically deposited silver detection substrate for surface-enhanced Raman spectroscopy cancer diagnostics. Journal of Biomedical Optics. 23(7), 075002. (2018)

95. Rashid, M.H, T.K. Mandal. Synthesis and Catalytic Application of Nanostructured Silver Dendrites. The Journal of Physical Chemistry C. 111(45), 16750-16760. (2007)

96. Wenya Cai, Xianghu Tang, Liangbao Yang, Xin Wang. Facile fabrication of leafy spikes-like silver dendrite crystals for SERS substrate. Materials Research Bulletin. 48(10), 4125-4133. (2013)

97. Shunping Xie, Xicui Zhang, Dan Xiao, Man Chin Paau, Jing Huang, Martin M. F. Choi. Fast Growth Synthesis of Silver Dendrite Crystals Assisted by Sulfate Ion and Its Application for Surface-Enhanced Raman Scattering. The Journal of Physical Chemistry C. 115(20), 9943-9951. (2011)

98. Feng-Zi Cong, Hong Wei, Xiao-Rui Tian, Hong-Xing Xu. A facile synthesis of branched silver nanowire structures and its applications in surface-enhanced Raman scattering. Frontiers of Physics.7(5), 521-526. (2012)

99. Huan Chen, Jianyong Luo, Tian Zeng, Long Jiang, Yuyang Sun, Zhifeng Jiao, Yong Jina, Xiaosong Sun. Investigation of the synthesis, SERS performance and application in glucose sensing of hierarchical 3D silver nanostructures. New Journal of Chemistry. 38(8), 3907-3916. (2014)

100. Youyi Xia, Tengjiao Li, Chan Gao, Cong Ma, Jun Chen. Facile fabrication of hierarchically flowerlike Ag microstructure for SERS application. Journal of Materials Science. 49(7), 2781-2786. (2014)

101. Yue Li, Michael Driver, Eric Decker, Lili He. Lipid and lipid oxidation analysis using surface enhanced Raman spectroscopy (SERS) coupled with silver dendrites. Food Research International. 58, 1-6. (2014)

102. Xia, Y.Y. and J.M. Wang, Hierarchical silver nano dendrites: One-step preparation and application for SERS. Materials Chemistry and Physics. 125(1-2), 267-270. (2011)

103. Gu, C., & Zhang, T. Y. Electrochemical synthesis of silver polyhedrons and dendritic films with superhydrophobic surfaces. Langmuir. 24(20), 12010-12016. (2008)

104. Qin, X., Miao, Z., Fang, Y., Zhang, D., Ma, J., Zhang, L., Shao, X. Preparation of dendritic nanostructures of silver and their characterization for electroreduction. Langmuir, 28(11), 5218-5226. (2012).

105. Mandke, M. V., Han, S. H., & Pathan, H. M. Growth of silver dendritic nanostructures via electrochemical route. CrystEngComm, 14(1), 86-89. (2012).

106. Bian, J., Shu, S., Li, J., Huang, C., Li, Y. Y., & Zhang, R. Q. Reproducible and recyclable SERS substrates: Flower-like Ag structures with concave surfaces formed by electrodeposition. Applied Surface Science, 333, 126-133. (2015).

107. Jiang, Z., Lin, Y., & Xie, Z. Structural investigations and growth mechanism of well-defined Ag dendrites prepared by conventional redox displacement. Materials Chemistry and Physics, 134(2-3), 762-767. (2012).

108. Ding, H. P., Xin, G. Q., Chen, K. C., Zhang, M., Liu, Q., Hao, J., & Liu, H. G. Silver dendritic nanostructures formed at the solid/liquid interface via electroless deposition. Colloids and Surfaces A: Physicochemical and Engineering Aspects, 353(2-3), 166-171. (2010).

109. Fang, J., You, H., Kong, P., Yi, Y., Song, X., & Ding, B. Dendritic silver nanostructure growth and evolution in replacement reaction. Crystal growth & design, 7(5), 864-867. (2007).

110. Ren, W., Guo, S., Dong, S., & Wang, E. A simple route for the synthesis of morphology-controlled and SERS-active Ag dendrites with near-infrared absorption. The Journal of Physical Chemistry C, 115(21), 10315-10320. (2011).

111. Wang, L., Li, H., Tian, J., & Sun, X. Monodisperse, micrometer-scale, highly crystalline, nanotextured Ag dendrites: rapid, large-scale, wet-chemical synthesis and their application as SERS substrates. ACS applied materials & interfaces, 2(11), 2987-2991. (2010).

112. Song, J., Hou, J., Tian, L., Guan, Y., Zhang, Y., & Zhu, X. X. Growth of giant silver dendrites on layer-by-layer assembled films. Polymer, 63, 237-243. (2015).

113. Forati-Nezhad, M., Sadeghi, G. M. M., Yaghmaie, F., & Alimohammadi, F. Affecting the morphology of silver deposition on carbon nanotube surface: From nanoparticles to dendritic (tree-like) nanostructures. Materials Science and Engineering: C, 46, 232-238. (2015).

114. Laurier, K. G., Poets, M., Vermoortele, F., De Cremer, G., Martens, J. A., Uji-i, H., Roeffaers, M. B. Photocatalytic growth of dendritic silver nanostructures as SERS substrates. Chemical communications, 48(10), 1559-1561. (2012).

115. Ahmed, I., Wang, X., Boualili, N., Xu, H., Farha, R., Goldmann, M., & Ruhlmann, L. Photocatalytic synthesis of silver dendrites using electrostatic hybrid films of porphyrin–polyoxometalate. Applied Catalysis A: General, 447, 89-99. (2012).

116. Wang, X., & Liu, X. Self-assembled synthesis of Ag nanodendrites and their applications to SERS. Journal of Molecular Structure, 997(1-3), 64-69. (2011).

117. Qiao, Y., Lin, Y., Wang, Y., Li, Z., & Huang, J. Metal-driven viscoelastic wormlike micelle in anionic/zwitterionic surfactant systems and template-directed synthesis of dendritic silver nanostructures. Langmuir, 27(5), 1718-1723. (2011).

118. Yang, C., Xie, Y. T., Yuen, M. M., Xiong, X., & Wong, C. P. A facile chemical approach for preparing a SERS active silver substrate. Physical Chemistry Chemical Physics, 12(43), 14459-14461. (2010).

119. Tang, S., Meng, X., Lu, H., & Zhu, S. PVP-assisted sonoelectrochemical growth of silver nanostructures with various shapes. Materials Chemistry and Physics, 116(2-3), 464-468. (2009).

120. Tang, S., Vongehr, S., & Meng, X. Two distinct branch–stem interfacial structures of silver dendrites with vertical and slanted branchings. Chemical Physics Letters, 477(1-3), 179-183. (2009).

121. Zhu, J., Liu, S., Palchik, O., Koltypin, Y., & Gedanken, A. Shape-controlled synthesis of silver nanoparticles by pulse sonoelectrochemical methods. Langmuir, 16(16), 6396-6399. (2000).

122. Zhou, Y., Yu, S. H., Wang, C. Y., Li, X. G., Zhu, Y. R., & Chen, Z. Y. A Novel ultraviolet irradiation photoreduction technique for the preparation of single-crystal Ag nanorods and Ag dendrites. Advanced Materials, 11(10), 850-852. (1999).

123. Xiaohu Xia, Yi Wang, Aleksey Ruditskiy, Younan Xia. 25th Anniversary Article: Galvanic Replacement: A Simple and Versatile Route to Hollow Nanostructures with Tunable and Well-Controlled Properties. Advanced Materials, 25(44), 6313-6333. (2013)

124. Zhang W, Tan F, Wang W, Qiu X, Qiao X, Chen J. Facile, template-free synthesis of silver nanodendrites with high catalytic activity for the reduction of p-nitrophenol. Journal of Hazardous Materials, 217, 36-42. (2012)

125. Jiang, Z.Y., Y. Lin, and Z.X. Xie, Structural investigations and growth mechanism of well-defined Ag dendrites prepared by conventional redox displacement. Materials Chemistry and Physics. 134(2-3), 762-767. (2012)

126. Audrius V. Avizienis, Cristina Martin-Olmos, Henry O. Sillin, Masakazu Aono, James K. Gimzewski, Adam Z. Stieg. Morphological Transitions from Dendrites to Nanowires in the Electroless Deposition of Silver. Crystal Growth & Design. 13(2), 465-469. (2013)

127. Wei-Han Hsiao, Hsin-Yu Chen, Yu-Cheng Yang, Yu-Liang Chen, Chi-Young Lee, Hsin-Tien Chiu. Surface-Enhanced Raman Scattering Imaging of a Single

Molecule on Urchin-like Silver Nanowires. ACS Applied Materials & Interfaces, 3(9), 3280-3284. (2011)

128. Hongyan Xu, Mingwang Shao, Tao Chen, Yi Zhao, Shuit-Tong Lee. Surface-enhanced Raman scattering on silver dendrite with different growth directions. Journal of Raman Spectroscopy, 43(3), 396-404. (2012)

129. Gaixia Zhang, Shuhui Sun, Mohammad Norouzi Banis, Ruying Li, Mei Cai, Xueliang Sun. Morphology-Controlled Green Synthesis of Single Crystalline Silver Dendrites, Dendritic Flowers, and Rods, and Their Growth Mechanism. Crystal Growth & Design, 11(6), 2493-2499. (2011)

130. Rongji Liu, Shiwen Li, Xuelian Yu, Guangjin Zhang, Ying Ma, Jiannian Yao, Bineta Keita, Louis Nadjo. Polyoxometalate-Assisted Galvanic Replacement Synthesis of Silver Hierarchical Dendritic Structures. Crystal Growth & Design, 11(8), 3424-3431. (2011)

131. Yunxia Zhang, Shaodong Sun, Xiaozhe Zhang, Linli Tang, Xiaoping Song, Zhimao Yang. Sulfate-ion-assisted galvanic replacement tuning of silver dendrites to highly branched chains for effective SERS. Physical Chemistry Chemical Physics, 16(35), 18918-18925. (2014)

132. Cheng, W.M., C.C. Wang, and C.Y. Chen. The influence of Ni nanoparticles and Ni (II) on the growth of Ag dendrites immobilized on the chelating copolymer membrane. Materials Chemistry and Physics, 137(1), 76-84. (2012)

133. Jixiang Fang, Bingjun Ding, Xiaoping Song, Yong Han. How a silver dendritic mesocrystal converts to a single crystal. Applied Physics Letters, 92(17). (2008.)

134. Hildebrandt, P., & Stockburger, M. Surface-enhanced resonance Raman spectroscopy of Rhodamine 6G adsorbed on colloidal silver. The Journal of Physical Chemistry, 88(24), 5935-5944. (1984).

135. Shende, C., Smith, W., Brouillette, C., & Farquharson, S. Drug stability analysis by Raman spectroscopy. Pharmaceutics, 6(4), 651–662. (2014)

136. William, R.V., Das, G.M., Dantham, V.R. et al. Enhancement of Single Molecule Raman Scattering using Sprouted Potato Shaped Bimetallic Nanoparticles. Scientific Report 9, 10771 (2019).

137. Chiung-Wen Hsieh; Pei-Ying Lin; Shuchen Hsieh. Improved surface-enhanced Raman scattering of insulin fibril templated colloidal gold nanoparticles on silicon. Journal of Nanophotonics Volume 6, Issue 1. (2012)

138. Gendi Fu, Da-Wen Sun, Hongbin Pu, Qingyi Wei. Fabrication of gold nanorods for SERS detection of thiabendazole in apple. Talanta 195(1), 841-849. (2019)

Biographical information

Sankgeeth Vennila Sigamani was born in Chennai, Tamil Nadu, India. He received his Bachelor of Engineering degree in Mechanical Engineering from the Shiv Subramaniya Nadar college of engineering currently known as Shiv Nadar University Chennai, Tamil Nadu, India in 2019. He published a research article in a book ‘Trends in Manufacturing and Engineering Management’ about the effect of input velocity in the output of Vertical Axis Wind Turbine which was presented at an international conference organized by Springers. The author then joined the University of Texas at Arlington’s Department of Materials Science and Engineering to conduct graduate studies as a master’s student, researching under Dr. Yaowu Hao. His research is associated with development of metal nanostructures SERS device for its real-world application. Sankgeeth has hands on experience with Raman spectroscopy, Scanning electron microscopy, sputtering system and XRD.